CM²

MAGAZINE

第 58 期

南方科技大学海洋磁学中心主编

https://cm2.sustech.edu.cn/

创刊词

　　海洋是生命的摇篮，是文明的纽带。地球上最早的生命诞生于海洋，海洋里的生命最终进化成了人类，人类的文化融合又通过海洋得以实现。人因海而兴。

　　人类对海洋的探索从未停止。从远古时代美丽的神话传说，到麦哲伦的全球航行，再到现代对大洋的科学钻探计划，海洋逐渐从人类敬畏崇拜幻想的精神寄托演变成可以开发利用与科学研究的客观存在。其中，上个世纪与太空探索同步发展的大洋科学钻探计划将人类对海洋的认知推向了崭新的纬度：深海（deep sea）与深时（deep time）。大洋钻探计划让人类知道，奔流不息的大海之下，埋藏的却是亿万年的地球历史。它们记录了地球板块的运动，从而使板块构造学说得到证实；它们记录了地球环境的演变，从而让古海洋学方兴未艾。

　　在探索海洋的悠久历史中，从大航海时代的导航，到大洋钻探计划中不可或缺的磁性地层学，磁学发挥了不可替代的作用。这不是偶然，因为从微观到宏观，磁性是最基本的物理属性之一，可以说，万物皆有磁性。基于课题组的学科背景和对海洋的理解，我们对海洋的探索以磁学为主要手段，海洋磁学中心因此而生。

　　海洋磁学中心，简称 CM^2，一为其全名"Centre for Marine Magnetism"的缩写，另者恰与爱因斯坦著名的质能方程 $E = MC^2$ 对称，借以表达我们对科学巨匠的敬仰和对科学的不懈追求。

　　然而科学从来不是单打独斗的产物。我们以磁学为研究海洋的主攻利器，但绝不仅限于磁学。凡与磁学相关的领域均是我们关注的重点。为了跟踪反映国内外地球科学特别是与磁学有关的地球科学领域的最新研究进展，海洋磁学中心特地主办 CM^2 Magazine，以期与各位地球科学工作者相互交流学习、合作共进！

　　"海洋孕育了生命，联通了世界，促进了发展"。21 世纪是海洋科学的时代，由陆向海，让我们携手迈进中国海洋科学的黄金时代

目 录

题目：葛坤朋，Wyn Williams, Lesleis Nagy, & Lisa Tauxe on G-cubed：磁不稳定区（Bad Boys）存在的第一个实验证据

作者：葛坤朋博士，山东泗水人，东华理工大学副教授，硕士研究生导师。研究方向为岩石磁学、古地磁学和磁法勘探。2014 年博士毕业于中国科学院地质与地球物理研究所进入现于东华理工大学固体地球物理系从事教学科研工作，分别于 2012 和 2018 年两次赴英国爱丁堡大学从事访问学者研究。目前作为项目负责人主持与完成国家自然科学基金项目 2 项，省级自然科学与教学项目 3 项。在 G-cubed、Science Bulletin、地球物理学报等学术期刊发表学术论文 10 余篇，申请国家发明专利 3 项。

摘要：地质样品中的磁性矿物可以记录数十亿年以来地磁场的变化，为研究地球的演化提供了一种途径。磁性矿物的记录能力随磁性颗粒粒径大小而变化，近年来学者认为中等粒径颗粒（SD 和 PSD（SV））具有较好的磁性记录能力，而两端最大（MD）和最小（SP-SD）颗粒的记录能力都有所下降。最近的微磁模拟研究表明，即使在以前被认为是良好记录的中等粒径尺寸（SD-SV）范围内，也存在一个不稳定区域，其特征尚未完全了解。这种预测对于古地磁研究的基本精度至关重要，因为通过识别和排除这种不稳定的磁记录，可以提高古地磁强度测定的精度。本研究为不稳定区（即磁不稳定区，其间颗粒俗称 Bad Boys）的存在提供了第一个实验证据。

简介：Nagy 等人（2017）最近报道了一个低磁稳定性的晶粒尺寸范围，它存在于 SD/SV 边界，对于等尺寸的磁铁矿晶粒，相当于~84 nm-100 nm 的晶粒尺寸。这种低稳定区的特点是具有多种可能的畴态，如难轴取向 SV（HSV）、易轴取向 SV（ESV）或易轴取向 SD 结构。值得注意的是，这些畴态之间的势垒足够小，以至于它们在室温下是不稳定的或只是弱稳定的。并且，不稳定带的位置和宽度取决于矿物学和颗粒形态。尽管这些不稳定带对古地磁观测的意义尚未完全了解，但它们可能通过诸如 cooling rate、aging effect 和 pTRM tail 等不良

效应（阻挡温度和解阻温度不同）降低古地磁记录可靠性。

然而，这种不稳定区域的晶粒尺寸范围窄，难以直接观测，其影响很难从样品的总剩磁中分离出来。一种可能的解决方案是选择样品的平均粒径接近磁铁矿的不稳定区，进行低温氧化实验。随着氧化过程的进行，颗粒中 SD、HSV 和 ESV 畴态的比例会发生变化。在微磁模拟中我们采用多相多层有限元方法，使用建模软件 MERRILL，在模型中加入氧化梯度，可与实验数据进行更真实的比较。结合多层模型，实验观测结果与磁不稳定区磁畴状态的快速变化相一致（图 1）。

本研究利用多层核壳模型进行了微磁模拟，研究了磁滞参数和磁畴结构与氧化状态的关系。结果表明，从 SD 到 SV，磁铁矿性质有一系列的变化，基于粒度分布的平均结果与实验数据在趋势值和绝对值上都有很好的一致性。这些结果有力地表明，磁滞参数随氧化状态的增加和骤减能够最好地由在 SD 和 ESV 晶粒尺寸范围之间的不稳定区附近发生的畴态的快速变化来解释（图 2）。虽然不稳定旋涡状态的狭窄区域在多大程度上可能导致古强度测定结果不佳存在很大的不确定性，但本文的实验观测表明，不稳定区域附近晶粒尺寸的畴态快速变化与实验观测一致，因此形成了第一个证据表明不稳定区会影响大块样品的磁性。以细颗粒为主的古地磁样品，如在冷却边缘和火山碎屑岩中发现的样品，尽管以SD颗粒为主，但可能无法免受多畴态效应的影响（磁不稳定区内的多畴态），这些效应通常与较大颗粒中预期的 MD 状态有关。由于 SD 颗粒和大多数 SV 颗粒都保留了可靠的磁记录，一种有效的磁不稳定区识别方法将能够提升从地质样品中提取准确古地磁信号的效率。
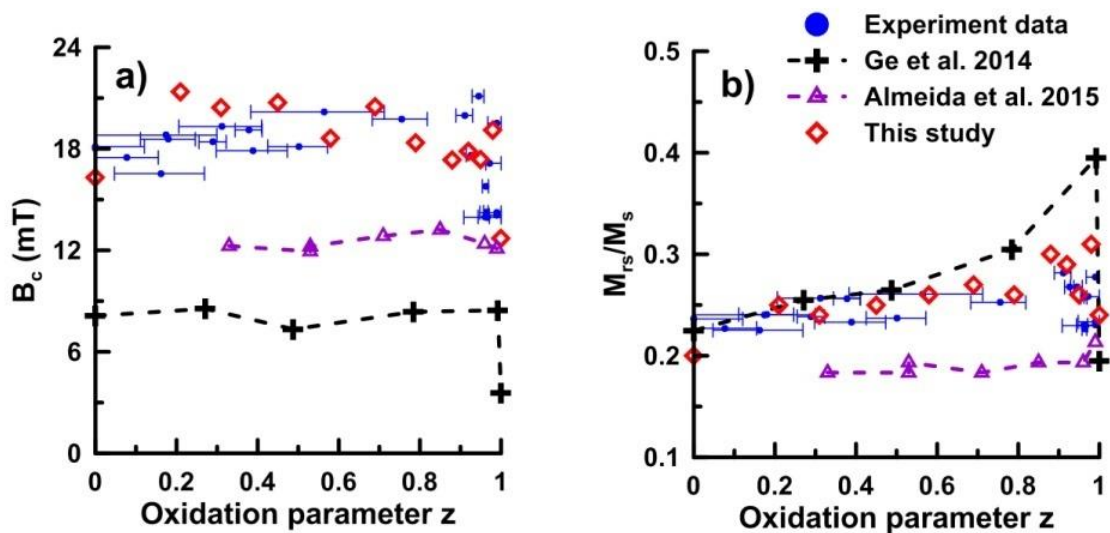
图1：（a）B_c和（b）M_{rs}/M_s与氧化参数（z）关系的实验结果及微磁模拟结果比较图，模型中都考虑了相互作用的影响。磁不稳定区域颗粒的氧化实验中出现磁滞参数随氧化程度先增后骤降的趋势，并且多层微磁模拟结果与实验结果相一致。
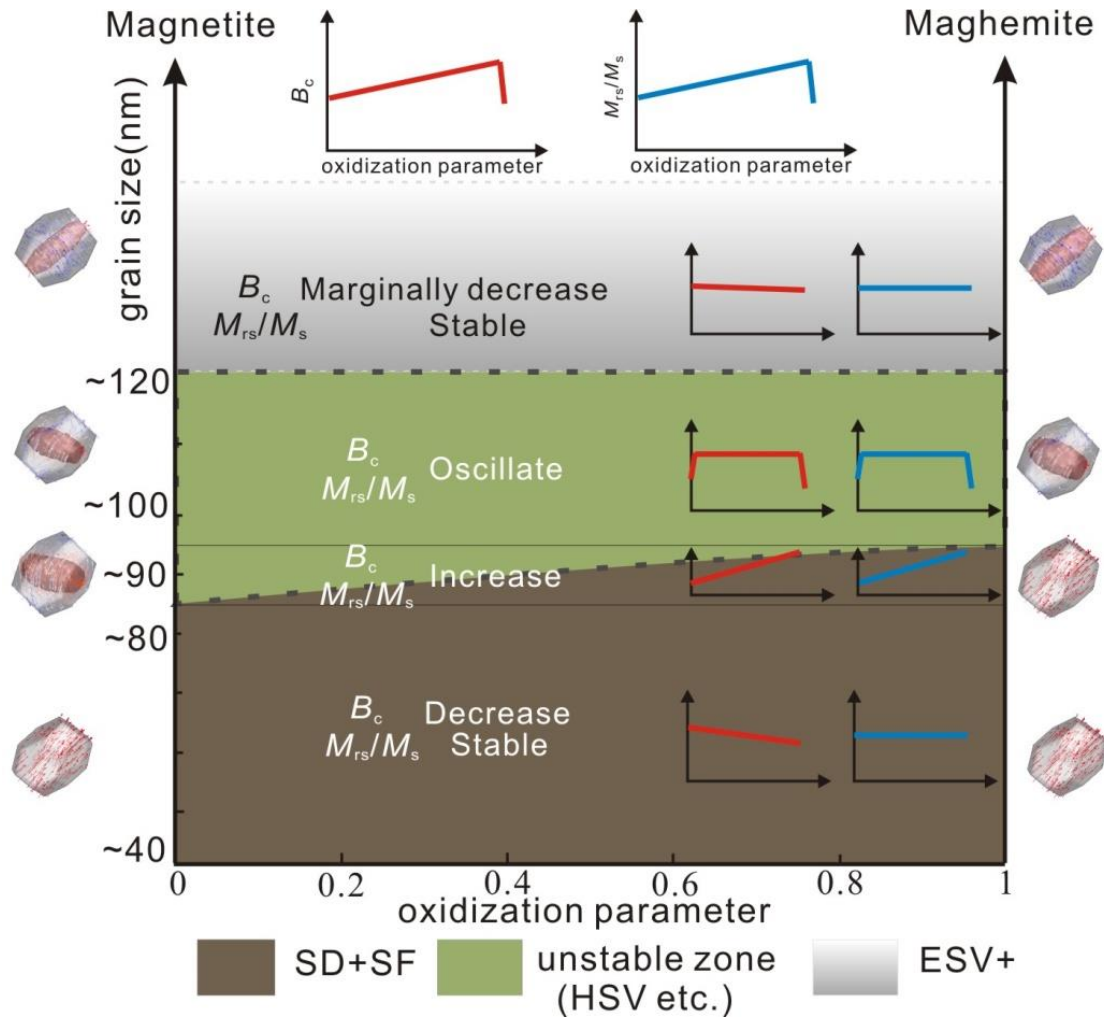

图2：磁赤铁矿化过程中不同粒径区域畴态变化图，淡黄色区域显示磁不稳定区在氧化过程中贡献的变化，并在宏观磁学参数中表现出来，即在磁滞参数随氧化程度变化图中出现先增后骤降的趋势。

1. 磁学手段研究新西兰古朗基俯冲带沿八字形主断层甲烷的流体积聚、迁移以及厌氧氧化

翻译人：张琪 zhangq7@sustech.edu.cn

摘要： 理解沿逆冲断层和八字形断层的流体流动轨迹对于理解加积系统的水利特性和断层机制有重要意义。我们利用岩石磁学手段结合背散射电子显像的方式描述了帕帕库断裂带内的磁性矿物的转化机制，断裂带位于北希古朗基边缘俯冲带上的八字形断层。断层岩心样品来自国际大洋发现计划第 375 航次，取于 U1518 点位。我们测试了室温下的岩石磁学参数，辅以一阶反转曲线和热磁曲线。约 60 米的帕帕库断层带包括两个主要的滑动带， 分别为上部主要脆性断裂带（304–321 mbsf）和下副断裂带（351–361 mbsf），以及一个中间带，被称为下部韧性变形区。主要脆性断层顶部的两个狭窄区域和下副断层上方的一个富沙层段中经历了强烈的磁性矿物成岩作用， 导致亚铁磁性的硫复铁矿重结晶形成顺磁性的黄铁矿。 我们认为，磁性矿物的次生成岩作用是在甲烷和硫酸盐同时存在的条件下，由厌氧甲烷的氧化驱动的。我们将观测到的变化与平行于断层的流体运输联系起来。上覆压实的含粘土的沉积物可能会阻碍的向上的平流通过断层带进入上盘。

ABSTRACT: Understanding the locus of fluid flow along thrust and splay faults is important to understand the hydraulic properties of accretionary systems and fault mechanics. Here, we use rock magnetic techniques in combination with backscattered electron imaging to depict the locus of enhanced magnetic mineral alteration within the Pāpaku fault, an active splay fault of the subduction interface at

the northern Hikurangi Margin. The Pāpaku fault was cored at Site U1518 during Expedition 375 of the International Ocean Discovery Program and we report room temperature magnetic parameters, complemented by first-order reversal and thermomagnetic curves in the depth interval 250–400 m below seafloor (mbsf). The ~60-m wide Pāpaku fault zone comprises two main slip zones, referred to as the upper main brittle (304–321 mbsf) and lower subsidiary (351–361 mbsf) fault zones, and an intervening zoned, termed the lower ductile deformation zone. Two narrow zones, at the top of the main brittle fault zone, and one in a sand-rich interval above the subsidiary fault zone, experienced enhanced magnetic mineral diagenesis, which resulted in the recrystallization of ferrimagnetic greigite to paramagnetic pyrite. We propose that secondary magnetic mineral diagenesis was driven by anaerobic methane oxidation within these intervals, which occurs in the presence of methane and sulfate. We relate the observed changes to the fault parallel transport of fluids which is restricted to two damage zones. Overlying compacted and clay-rich sediments likely act as a barrier to upward advective flow through the fault zone and into the hanging wall.
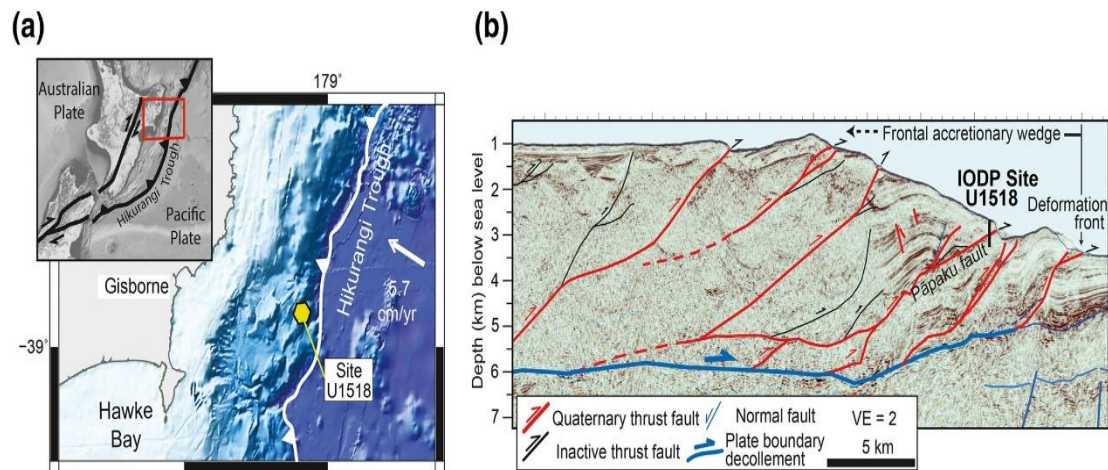

Figure 1. (a) Location and geotectonic setting of the Hikurangi subduction margin and the New Zealand plate boundary (inset). Displayed in the bathymetric map of the northern Hikurangi subduction margin are also the deformation front, IODP Site U1518 and the relative plate convergence vector. (b) Seismic cross section of the frontal accretionary wedge near the drilling transect of IODP Expedition 375, including interpretation after Barker et al. (2018). The location of IODP Site U1518 and trace of the Pāpaku fault are indicated. Figure modified from (Fagereng et al., 2019; Greve et al., 2020). IODP, International Ocean Discovery Program.
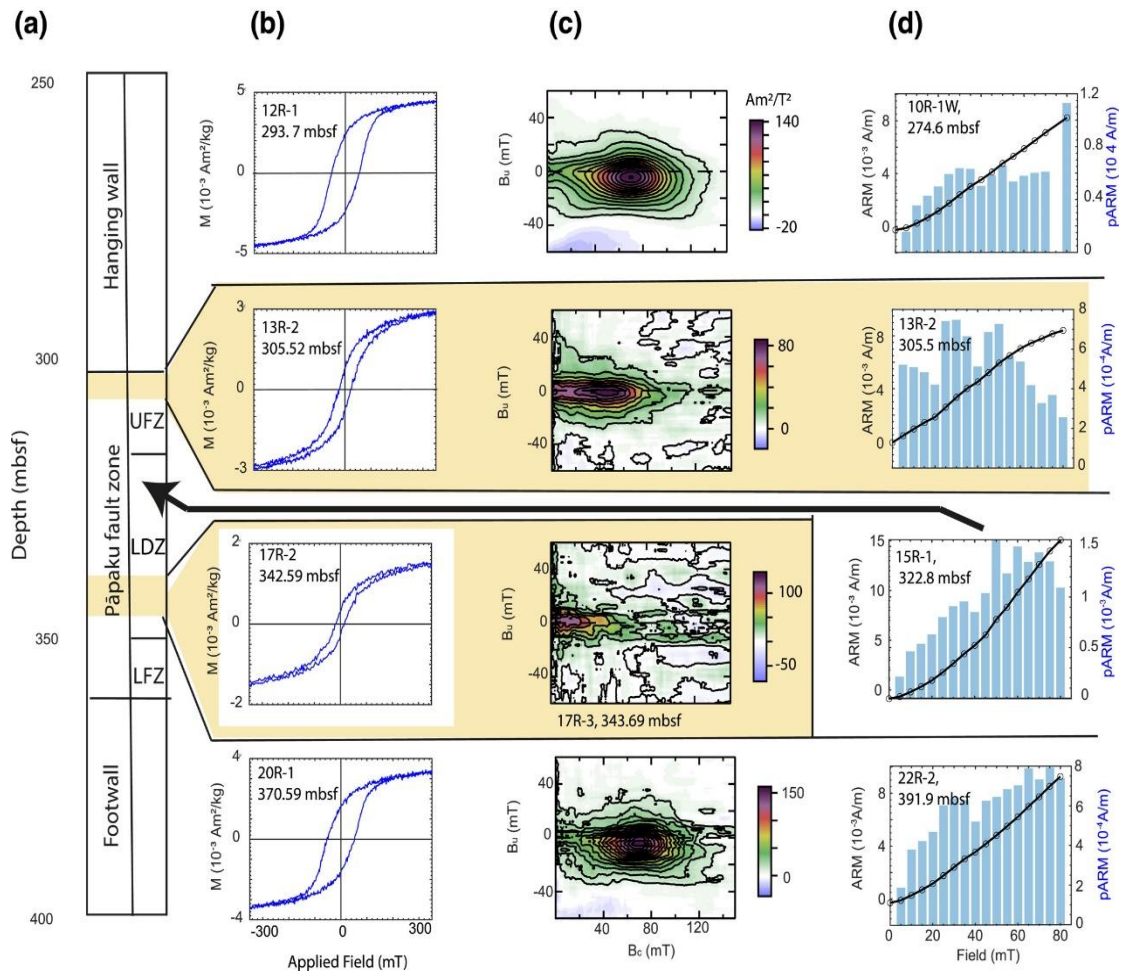
Figure 2. Representative rock magnetic properties of samples from hanging- and footwall (top and bottom rows, respectively) and from two intervals within the Pāpaku fault zone that yield anomalous magnetic properties. (a) Structural domains of the Pāpaku fault zone, where UFZ—upper main brittle fault zone, LDZ—lower ductile deformation zone, LFZ—lower subsidiary fault zone. (b) Hysteresis loops after slope correction (saturation field of 1 T). (c) First-order reversal curve (FORC) diagrams. (d) Anhysteretic remanent magnetization (ARM) acquisition curves (black line), and partial ARM (pARM) acquired at each treatment step (light blue columns). Sample identifiers and depth information are displayed in the top left corner of the hysteresis loop panels. See text for details.

2 标量磁力仪搭载小型 AUV 的磁力探测和目标体自主重采集

翻译人：李园洁 liyj3@sustech.edu.cn

摘要：本文介绍开发的一种标量磁力仪装备，并将其集成到两人便携式自主水下航行器 (AUV) 上用于地球物理和考古勘探。这种微型系统可采集到来自一种总场观测的几何微加工原子磁力仪的观测数据。传感器的数据可以保存用作前处理，同时传输到机载自主设备来实时感应和做出反应。这个系统已在可控的实验条件和海上确定其性能的极限。开发磁力仪数据的处理方法来校正来自 AUV 平台的干扰和误差以提高感测性能。进行海底调查时，在 AUV 上可实时探测和显示目标体的特征。这个系统可同时让单个或多个装备进行目标体自主重采集。综合平台上探测和目标体自主重采集的能力极大提高了基于 AUV 磁感应系统的勘探覆盖率。

ABSTRACT：A scalar magnetometer payload has been developed and integrated into a two-man portable autonomous underwater vehicle (AUV) for geophysical and archeological surveys. The compact system collects data from a Geometrics microfabricated atomic magnetometer, a total-field atomic magnetometer. Data from the sensor is both stored for post-processing and made available to an onboard autonomy engine for real-time sense and react behaviors. This system has been characterized both in controlled laboratory conditions and at sea to determine its performance limits. Methodologies for processing the magnetometer data to correct for interference and error introduced by the AUV platform were developed to improve sensing performance. When conducting seabed surveys, detection and characterization of targets of interest are performed in real-time aboard the AUV. This system is used to drive both single- and multiple-vehicle autonomous target reacquisition behaviors. The combination of on-board target detection and autonomous reacquire capability is found to increase the effective survey coverage rate of the AUV-based magnetic

sensing system..

**Figure 1**. Sensor system in long housing attached to REMUS 100 autonomous underwater vehicle
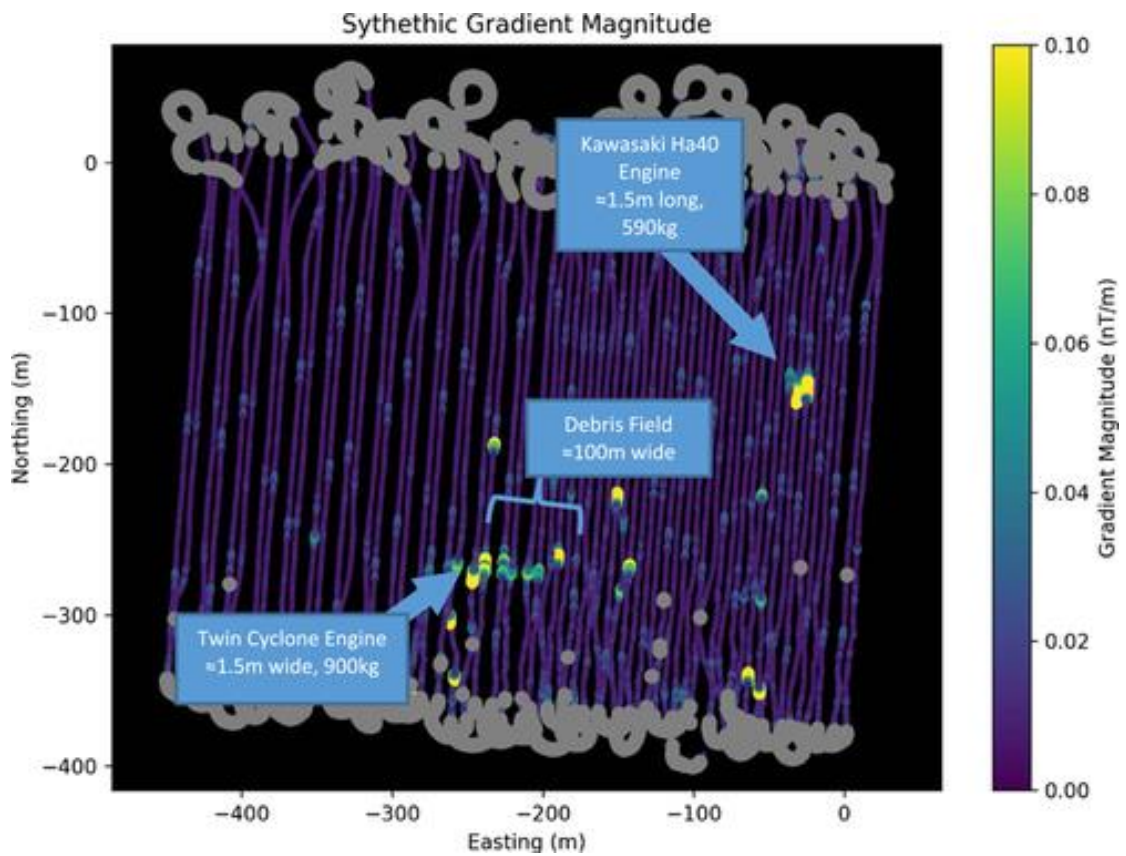
Figure 2. Processed synthetic gradient data from systematic magnetic survey over World War II archeological targets near Hansa Bay, Papua New Guinea. Debris from two aircraft wrecks generates strong signatures in the synthetic gradient. Subsequent surveys with sidescan sonar, optical imagers, and

divers identified the wreckage of a Japanese Ki-61 aircraft with a Kawasaki Ha40 engine and a U.S. B-25 Mitchell aircraft with a Wright R-2600 engine visible (the second engine of this twin-engine craft was not found). These targets are highlighted in the figure. "Blanked" data that has been rejected due to a high turn rate or invalid heading rate is shown in gray. The periodic "noise" in the gradient is interference from the acoustic modem system, which is not removed by this signal processing chain.
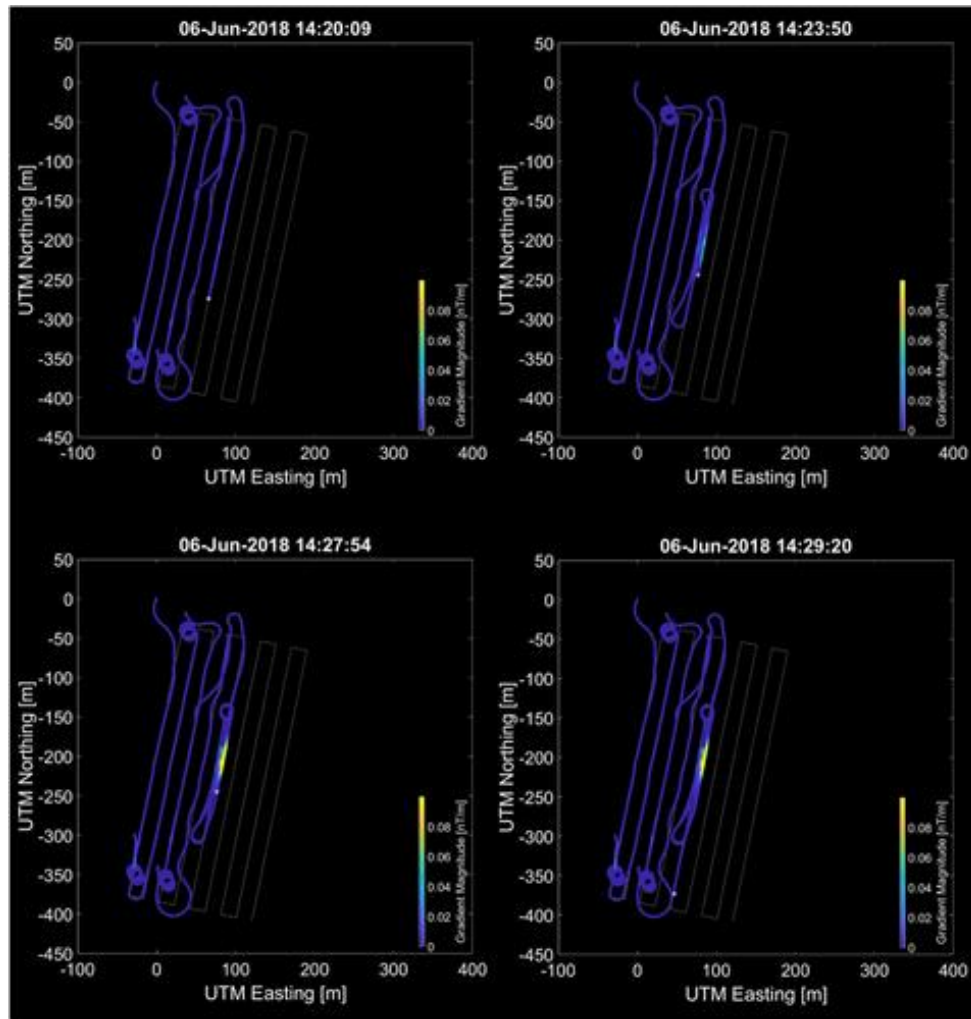
Figure 3. Autonomous reacquire behavior mission playback from a mission over an aircraft debris field. Time flows left to right, top to bottom. Gray lines show the planned mission track. The vehicle position is shown as a white dot. Top-left: The vehicle is running a broad survey pattern. Top-right: A target was detected, and the vehicle is running Reacquire Find maneuvering. Bottom-left: Detections were made in Reacquire Find, so the vehicle begins Reacquire Characterize maneuvering, centered over the correctly-resolved target position. Bottom-right: Reacquire Characterize maneuvering is complete, and the vehicle has resumed the broad survey path.

3. 地幔中的放射性热导致太古宙的海底随年龄的增长而变浅

翻译人：冯婉仪 fengwy@sustech.edu.cn

摘要：由于地质资料的缺乏，人们对太古宙地球地貌的了解很有限。尽管大陆地壳可能在 40 亿年之前和现在的一样大，但它被淹没或出露的程度尚不清楚。了解早期地球陆地出露数量的一个关键因素是大洋岩石圈的演化。尽管现今的大洋岩石圈随着年龄的增长而逐渐下沉，但根据地幔对流的数值模型，我们发现太古宙地幔中放射性同位素浓度较高，这使得地幔内能热较高，从而阻止了大洋岩石圈下沉，并可能导致海底在 25 亿年之前随年龄的增长而变浅。在这种情况下，以火山岛和重新浮出海面的海山或海洋高原形式出现的陆块可以长时间地出露在地表上，并且可能是太古宙唯一稳定的干旱陆块。因此，我们的研究结果允许重新评估生命起源的可能地点，因为它们支持了一个现有的假设，即生命起源于陆地而不是海洋环境。

ABSTRACT: Given the scarcity of geological data, knowledge of Earth's landscape during the Archaean eon is limited. Although the continental crust may have been as massive as present by 4 Gyr ago, the extent to which it was submerged or exposed is unclear. One key component in understanding the amount of exposed landmasses in the early Earth is the evolution of the oceanic lithosphere. Whereas the present-day oceanic lithosphere subsides as it ages, based on numerical models of mantle convection we find that higher internal heating due to a larger concentration of radioactive isotopes in the Archaean mantle halted subsidence, possibly inducing seafloor shallowing before 2.5 Gyr ago. In such a scenario, exposed landmasses in the form of volcanic islands and resurfaced seamounts or oceanic plateaus can remain subaerial for extended periods of time, and may have provided the only stable patches of dryland in the Archaean. Our results therefore permit a re-evaluation of possible locations for the origin of life, as they provide support to an existing hypothesis that suggests that life had its origins on land rather than in an oceanic environment.
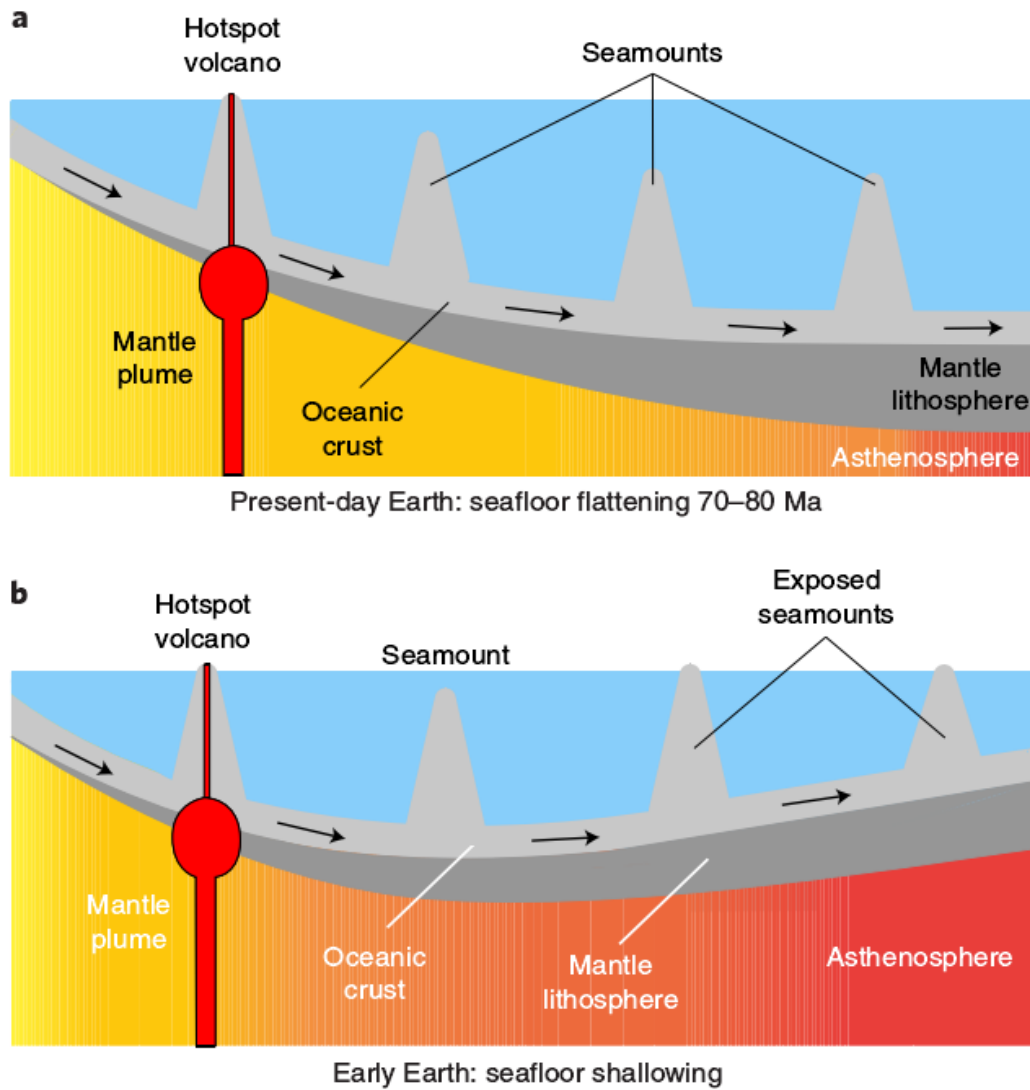
Figure 1. Bathymetric evolution of oceanic lithosphere at present and in the early Earth. a, At present, seafloor subsides as the plate moves away from mid-ocean ridge. Hotspot volcanism forms oceanic islands that eventually become seamounts as the plate subsides. Low concentration of heat-producing elements in the mantle lead to a moderate increase in temperature (yellow–red shading). b, In the early Earth, the concentration of heat-producing elements in the mantle was considerably higher than present, leading to a greater temperature increase. As at present, oceanic islands may become seamounts, but additional heating can lead to seafloor shallowing and allow seamounts to resurface.

4. 新生代大气 CO_2、风化输入和碳酸盐补偿深度的协调机制

翻译人：仲义 zhongy@sustech.edu.cn

摘要：新生代（66 到 0 百万年间）表现为碳循环的长期异常和大的气候转型变化，其中一些变化对当前碳循环动力学的理解产生挑战。作者采用了一种全新的方法，以成熟的海洋碳酸盐化学模型来研究导致观测到长期趋势发生的可能机制。利用二氧化碳的分压、PH 值以及碳酸盐补偿深度观测记录以及一系列的模拟结果，作者找到调控新生代气候变化和 CCD 长期变化的趋势。作者认为 CCD 的响应变化与硅酸盐和碳酸盐风化速率解耦，进而与大陆隆起假说发起挑战。影响脱耦变化的主要机制主要是陆架-盆地碳酸盐埋藏分馏和远洋钙质沉积物的扩散。作者认为温度效应对海洋有机质再矿化速率的影响在控制碳循环动力学方面起着关键作用，特别是新生代变暖时期。

ABSTRACT: The Cenozoic era (66 to 0 million years) is marked by long-term aberrations in carbon cycling and large climatic shifts, some of which challenge the current understanding of carbon cycle dynamics. Here, we investigate possible mechanisms responsible for the observed long-term trends by using a novel approach that features a full-fledged ocean carbonate chemistry model. Using a compilation of pCO_2, pH, and calcite compensation depth (CCD) observational evidence and a suite of simulations, we reconcile long-term Cenozoic climate and CCD trends. We show that the CCD response was decoupled from changes in silicate and carbonate weathering rates, challenging the continental uplift hypothesis. The two dominant mechanisms for decoupling are shelf-basin carbonate burial fractionation combined with proliferation of pelagic calcifers. The temperature effect on remineralization rates of marine organic matter also plays a critical role in controlling the carbon cycle dynamics, especially during the warmer periods of the Cenozoic.
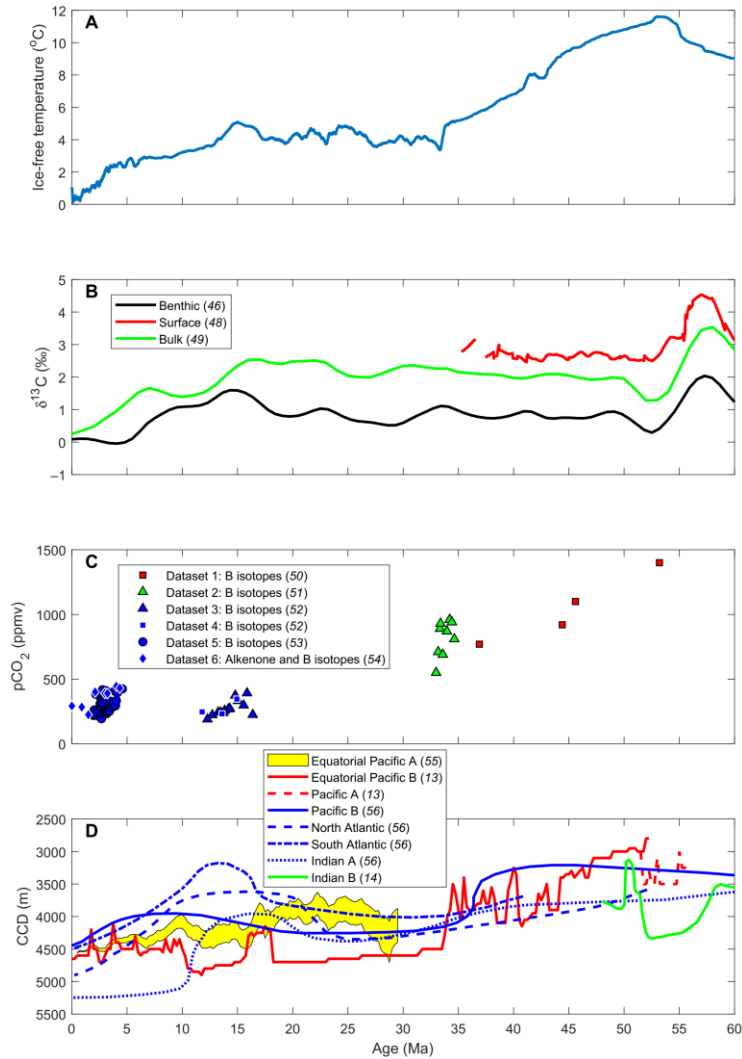
Figure 1. Compilation of Cenozoic temperature, $\delta^{13}C$, pCO_2, and calcite compensation depth (CCD) history for different ocean basins. (A) The reconstructed deep ocean temperature across the Cenozoic is based on the $\delta^{18}O$ data from (46). The prescribed temperature change in the model is based on the $\delta^{18}O$-temperature relationship described in (47): Tt = 16.9 - 4.0 × ($\delta18Ot$ - $\delta18Osw$), where $\delta^{18}O_t$ is the observed data and $\delta^{18}Osw$ is the $\delta^{18}O$ of the seawater at a given time in the past (B) $\delta^{13}C$ compilation at different depths [benthic, (46); surface, (48); bulk, (49)] and (C) atmospheric CO_2 reconstruction based on paleo-proxies from multiple sources: dataset 1 (50), dataset 2 (51), dataset 3 (52), dataset 4 (52), dataset 5 (53), dataset 6 (54), and expressed in parts per million by volume. (D) Pacific, Atlantic, and Indian Ocean CCD expressed in meters below sea level. Equatorial Pacific A compiled from (55); Equatorial Pacific B and Pacific A from (13); Pacific B, North Atlantic, South Atlantic, and Indian A from (56); and Indian B from (14). Hydrothermals are excluded from the original Indian Ocean CCD data (green line) (14).
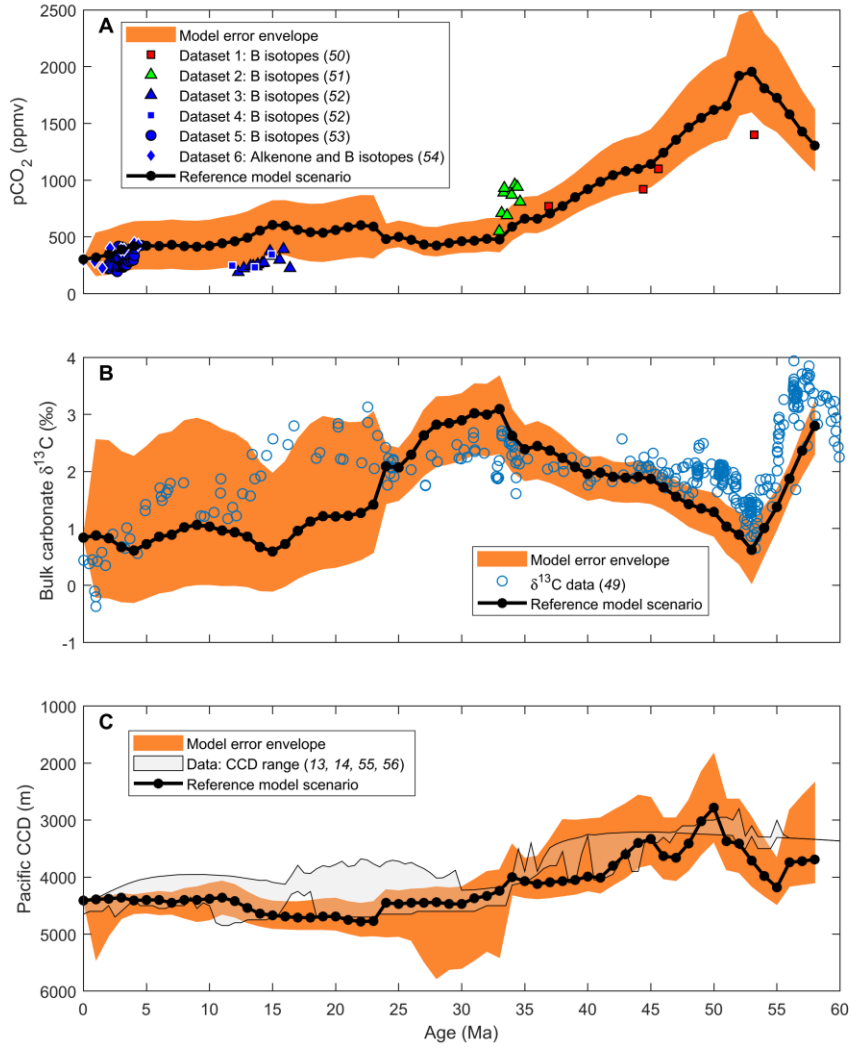
10

Figure 2. The reference model simulation (black line with closed black circles) and error envelope (orange area) plotted against the paleo-proxy data displayed and described in Fig. 1. (A) Atmospheric pCO^2 predicted by the model in parts per million by volume. (B) Model predicted sediment bulk carbonate δ^{13}C versus the observed sediment data [open blue circles, (49)]. ‰, per mil. (C) Model predicted evolution of the Pacific CCD against the Pacific CCD data range displayed in Fig. 1. The orange area represents model results for a 95% confidence interval of the Martin curve temperature dependence and the uncertainty associated with the GEOCARB weathering parameters (57). The Martin curve temperature dependence is as follows: b(t) = 0.062 × T(t) + 0.303(± 2σ), where b(t) is the Martin curve attenuation coefficient at time t, and T is the median water temperature of the upper 500 m of the water column at time t. σ (0.16, calculated in this study) is the SD of residuals (disagreement between the linear regression model and the dataset), and 2σ is the 95% confidence interval.
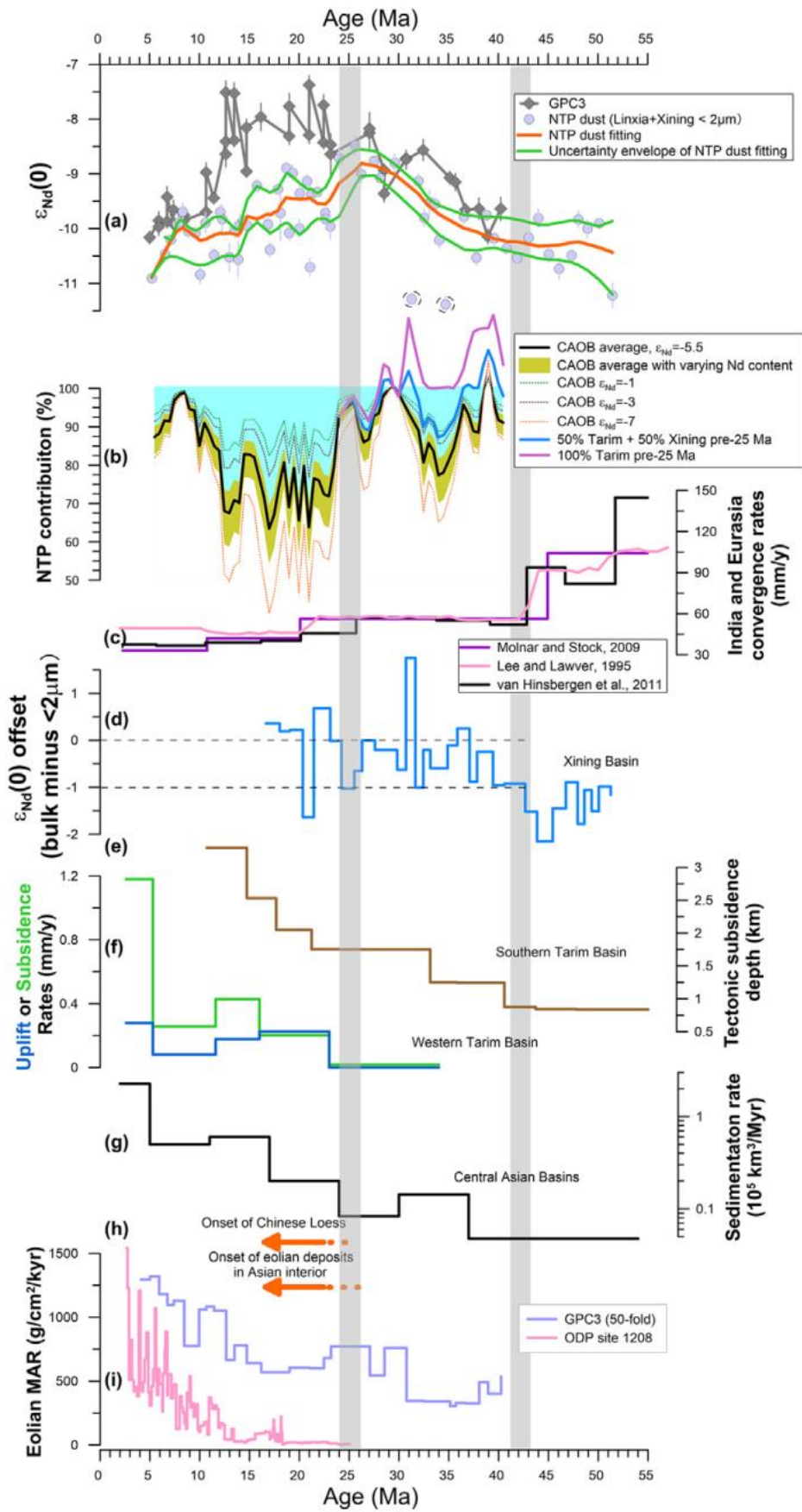
Figure 3. The reconstructed Cenozoic eolian dust Nd isotopic variations (expressed in eNd(0) values) in the NTP and their comparison with other records. (a) Dust eNd(0) values in the NTP and core GPC3. For the NTP, the bold orange curve represents the locally weighted scatterplot smoothing (LOWESS, smoothing factor is 0.15) fitting of the NTP dust data from the Nd isotopic compositions of the < 2 lm fraction in the Linxia and Xining Basins, and the green curve represents the uncertainty envelope (note that the two very negative data with dashed circles at 30– 36 Ma have been excluded for the composite curve). (b) The NTP contributions to the NPO dust estimated by mass balance by equation (1) using NTP and NPO records and assuming a constant CAOB Nd composition in various scenarios (CAOB eNd values of 1, 3, 7, and 5.5). The black line denotes the NTP contribution estimated by the eNd mean value of 5.5 for the < 2 lm fraction of the CAOB surface sediments (Table S3). The yellow shaded area shows the uncertainty envelope of varying Nd concentrations (1r change in Nd mean concentration of < 2 lm fraction of the CAOB surface sediments, from 24 to 46 lg/g, Table S3) corresponding to CAOB eNd values of 5.5. The CAOB contribution of the western Tarim Basin (for the period between 38 and 30 Ma) to NPO dust is shown by the light blue area. Two sensitivity tests for the Tarim Basin contribution before 25 Ma are shown in the bold blue (Tarim Basin represents 100% of the NTP contribution) and violet lines (Tarim Basin represents 50% of the NTP contribution). (c) Convergence rates between India and Eurasia (Lee and Lawver, 1995; Molnar and Stock, 2009; van Hinsbergen et al., 2011). (d) Offset in the eNd(0) values between the bulk sediment and the < 2 lm fraction in the XJ section of the Xining Basin. (e) Tectonic subsidence depth in the Aertashi section in the western Tarim Basin (Blayney et al., 2019). (f) Average uplift (blue line) and subsidence (green line) rates in the southern Tarim Basin (Jiang and Li, 2014). (g) Sediment accumulation rate in central Asia (Me´tivier and Gaudemer, 1999). (h) The onset of eolian sediment development (orange arrows) in central Asia (Sun et al., 2010; Zheng et al., 2015) and in the CLP (Guo et al., 2002; Qiang et al., 2011). (i) Eolian mass accumulation rate (MAR) at DP site 1208 (Zhang et al., 2016) and in core GPC3 (Janecek and Rea, 1983). To show the variations in the two records on the same graph, the GPC3 data have been blown up 50 times. The vertical gray bars mark the two transition periods of 42 Ma and 25 Ma. For interpretation of the references to color in this figure legend, he reader is referred to the web version of this article.)
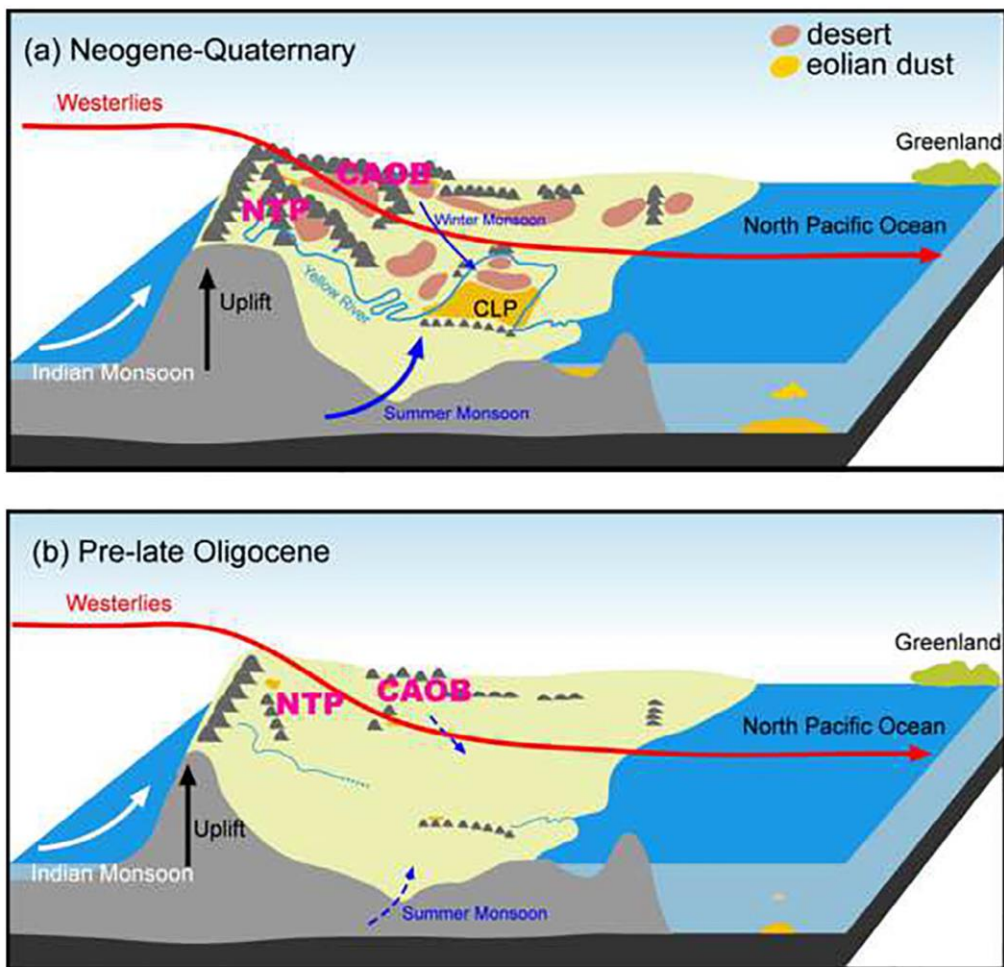
Figure 4. Schematic diagram of Asian dust production and transport from the NTP and CAOB regions to the proximal CLP, the distal North Pacific and even Greenland. (a) The Neogene-Quaternary regime (modified after Chen and Li, 2011 with tectonically active NTP and CAOB egions in combination with a strong East Asian monsoon system). (b) The regime prior to the late Oligocene (further modified from (a) with igh elevations in south-central Tibet but a less tectonically active NTP and a relatively low-relief CAOB).

5. 中国岩石圈长波磁场

翻译人：曹伟 11930854@QQ.com

摘要：本文结合卫星模型 CHAOS-6、MF7、LCS-1 和 NGDC720 提供的长波长信息，以及 97994 个航磁短波长数据（10km × 10km 分辨率）的高质量汇编，提出了中国岩石圈场的区域新模型 CLAS。模型是使用以中国为中心的全球球谐函数的衰减原理进行估算的。CLAS 模型确定包含谐度高达 400。虽然为了平衡数据集的一致性，航磁数据失去了一定的精度，但是结果表明 CLAS 模型与卫星模型在低阶项下具有很高的相关性（相关度 > 0.9），而在高阶项下的相关性更强，反映了中国大陆岩石圈场的更多特征,完善的区域实例包括长白山、四川盆地和青藏高原。CLAS 模型与中国航磁资料在波长约 100km（对应球谐度 n = 400）处具有良好的一致性（相关性>0.9），填补了卫星模型与航磁资料之间的空白。与 100 公里处过滤的航磁数据进行比较，得到了很好的一致性（相关性 > 0.95）。CLAS 模型与航磁数据之间的残差仍然很大（rms > 70nt），但大部分失配是由波长较短的场引起的，模型在 400 度以下无法拟合；通过增加模型阶数可以减少这种失配。我们提供了一个地质实例来反映卫星数据的加入是如何改变从磁信息中得出的地质结论。但是，这两个数据集并不完全一致，未来的模式应该从航磁数据的重新分析及其测线调平开始，以确保与卫星模式的一致性。

ABSTRACT: We present new regional models, denoted CLAS, of the Chinese lithospheric field, combining the long-wavelength information provided by satellite-derived models: CHAOS-6, MF7, LCS- 1 and NGDC720, and an extremely high-quality compilation of 97 994 aeromagnetic survey data with 10 km × 10 km resolution for shorter wavelength. The models are estimated using a depleted basis of global spherical harmonic functions centred on China. CLAS models are determined include harmonic degrees up to 400. Although some accuracy of aeromagnetic data is

lost in order to balance the consistent of two data sets, the results show that CLAS models have a high correlation with the satellite models at low-degree terms (degree correlation > 0.9) but with more power at high-degree terms, reflecting more features of the lithospheric field in continental China. Examples of improvement include Changbai mountains, Sichuan Basin and Qinghai–Tibet Plateau. CLAS models have good agreement (coherence > 0.9) with Chinese aeromagnetic data at wavelength down to about 100 km (corresponding to spherical harmonic degree n = 400), filling the usual gap between satellite models and aeromagnetic data. Comparison with aeromagnetic data filtered at 100 km gives good agreement (correlation > 0.95). The residuals between CLAS models and aeromagnetic data are still large (rms > 70 nT), but with most of misfits arising from shorter wavelength fields that the model cannot fit at degree up to 400; such misfit could be reduced by increasing the model degree. We provide a geological example of how the inclusion of satellite data can change the geological conclusions that can be drawn from the magnetic information. However, the two data sets are not completely consistent, future models should start from a reanalysis of the aeromagnetic data and its line levelling to ensure consistency with the satellite model.
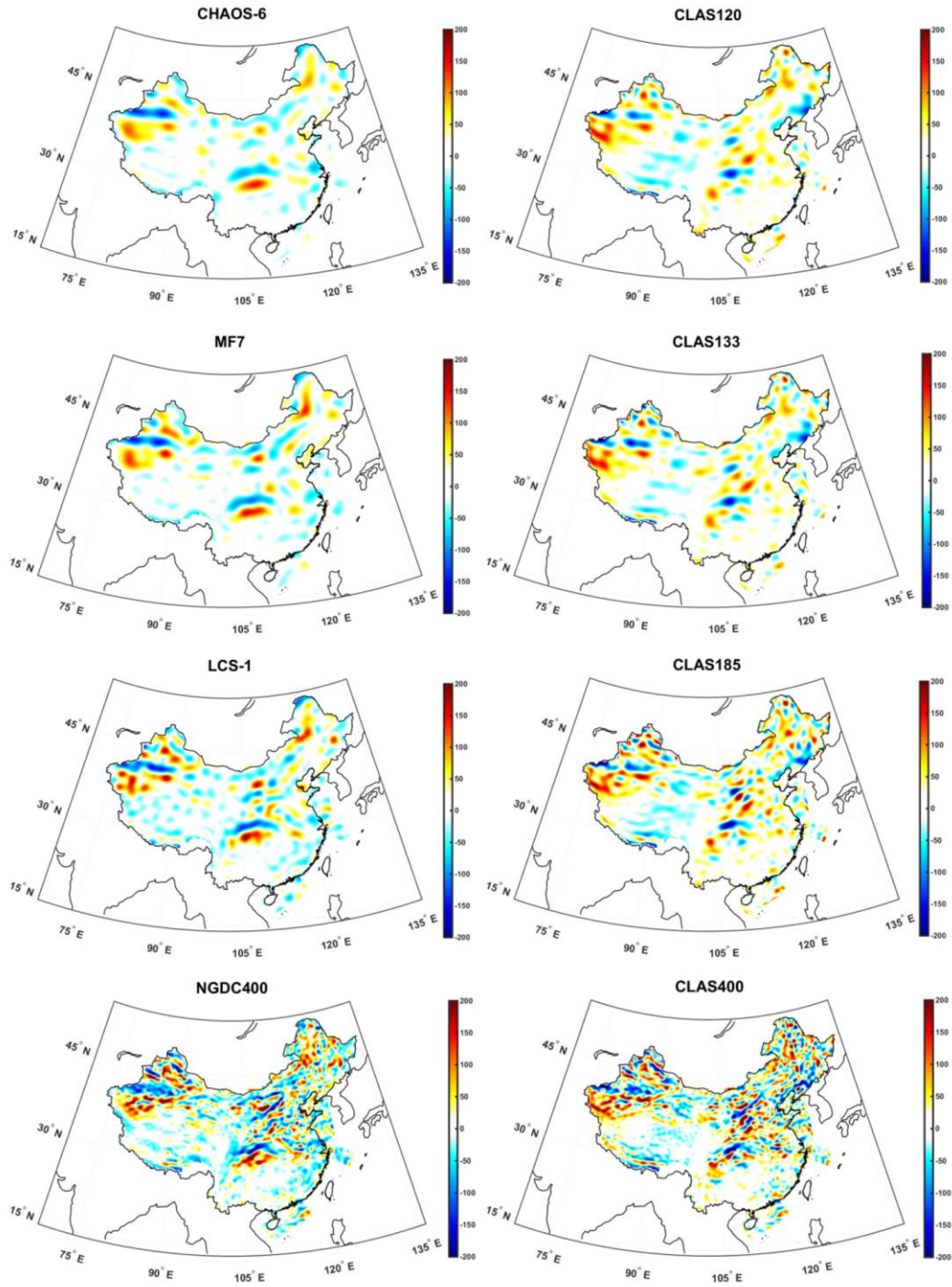
Figure 1. Lithospheric magnetic field maps of scalar anomaly F in continental China at a reference Earth surface datum. Units are nT. Top panel: from CHAOS-6 (left) and CLAS120 (right) for SH degrees up to 120. Second panel: from MF7 (left) and CLAS133 (right) for SH degrees up to 133. Third panel: from LCS-1 (left) and CLAS185 (right) for SH degrees up to 185. Bottom panel: from NGDC (left) and CLAS400 (right) for SH degrees up to 400.

6. 俯冲方向逆转导致的汇聚型大陆边缘的板内破裂和板缘破裂:南海边缘的数值模拟研究

翻译人：刘伟 inewway@163.com

摘要: 汇聚型板块边缘的破裂被认为是板片回滚导致的弧后扩张或者俯冲方向逆转引起的拖曳作用的结果。虽然板片回滚假说已经进行了深入的研究，但我们对俯冲方向逆转作用的认识仍然有限。利用基于南海区域的热力学模拟，研究了俯冲方向的逆转是如何控制汇聚型边缘破裂的。数值模拟结果表明，汇聚型边缘的成熟度和大洋岩石圈的年龄决定了两种不同的破裂模式，即板内破裂和板缘破裂。对一个~15- ~45 Ma 的俯冲板片，俯冲持续时间的增加有利于板内破裂，即一大块大陆物质从上冲板块中分离。相反，当俯冲是一个持续时间较短的事件时，有利于板缘破裂，出现一个较不连续的大陆碎片和俯冲板片撕裂的宽区域。这两种模式符合南海西部和东部的裂陷特征，表明古南海西北方向俯冲的持续时间不同可能是沿南海边缘走向产生不同破裂特征的原因。此外，我们的结果也暗示了在现今南海地区还可能存在一条与西北方向俯冲有关的两段海沟。

ABSTRACT: The dynamics of continental breakup at convergent margins has been described as the results of backarc opening caused by slab rollback or drag force induced by subduction direction reversal. Although the rollback hypothesis has been intensively studied, our understanding of the consequence of subduction direction reversal remains limited. Using thermo-mechanical modeling based on constraints from the South China Sea (SCS) region, we investigate how subduction direction reversal controls the breakup of convergent margins. The numerical results show that two distinct breakup modes, namely, continental interior and edge breakup ("edge" refers to continent above the plate boundary interface), may develop depending on the "maturity" of the convergent margin and the age of the oceanic lithosphere. For a slab age of ~15 to ~45 Ma, increasing the

duration of subduction promotes the continental interior breakup mode, where a large block of the continental material is separated from the overriding plate. In contrast, the continental edge breakup mode develops when the subduction is a short-duration event, and in this mode, a wide zone of less continuous continental fragments and tearing of the subducted slab occur. These two modes are consistent with the interior (relic late Mesozoic arc) and edge (relic forearc) rifting characteristics in the western and eastern SCS margin, suggesting that variation in the northwest-directed subduction duration of the Proto-SCS might be a reason for the differential breakup locus along the strike of the SCS margin. Besides, a two-segment trench associated with the northwest-directed subduction is implied in the present-day SCS region.
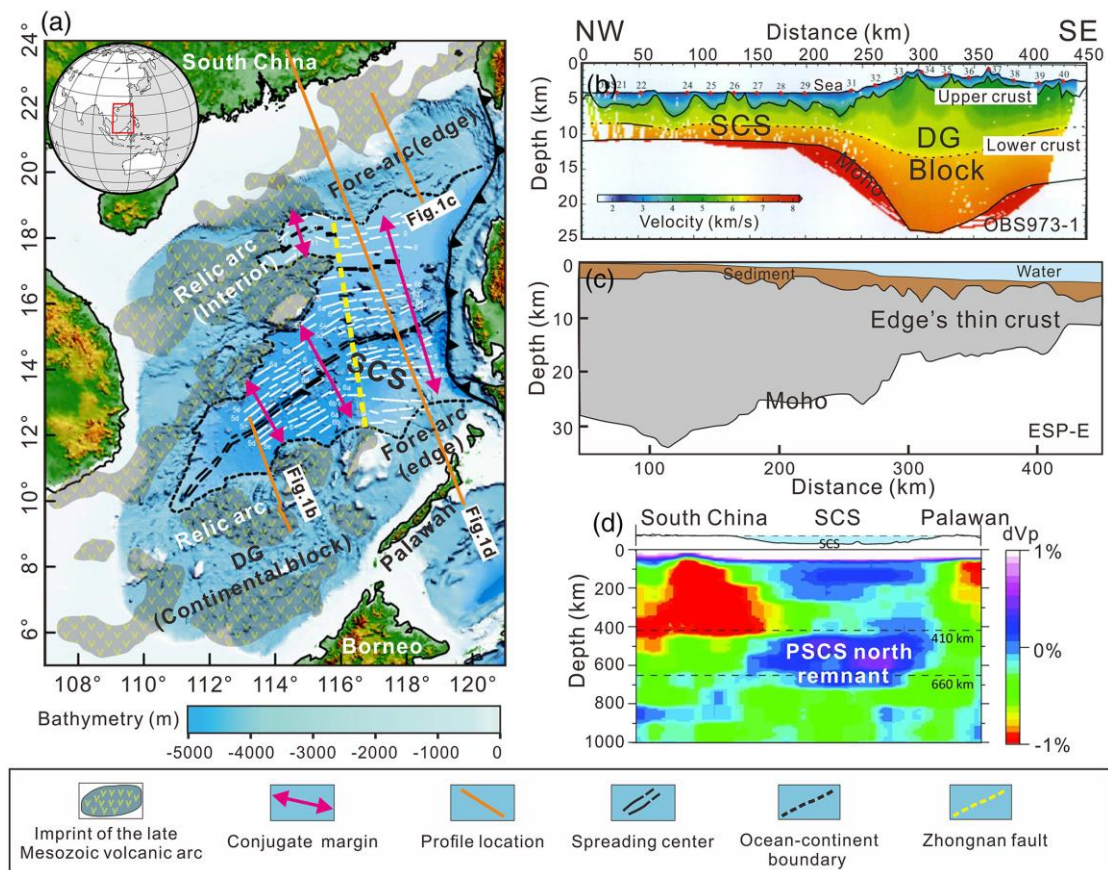

Figure 1. Observations in the South China Sea region. (a) Bathymetry map and the imprint of the late Mesozoic volcanic arc in the SCS region. The imprint of the late Mesozoic volcanic arc shows that the Cenozoic opening of the SCS basins has broken the continental interior in the west and the continental edge in the east (Li, Sun, & Yang, 2018). (b and c) Crustal velocity structures beneath the southwestern

and northeastern margin (Nissen et al., 1995; Qiu et al., 2011). For more crustal structures in SCS, please refer to OBS2001 in Zhao et al. (2010) and OBS2006 in Wei et al. (2011). (d) Tomographic section indicating a subhorizontal fast slab anomaly (the PSCS north slab) under the east SCS (Sun et al., 2019; Wu & Suppe, 2018). DG: Dangerous Grounds (Nansha).
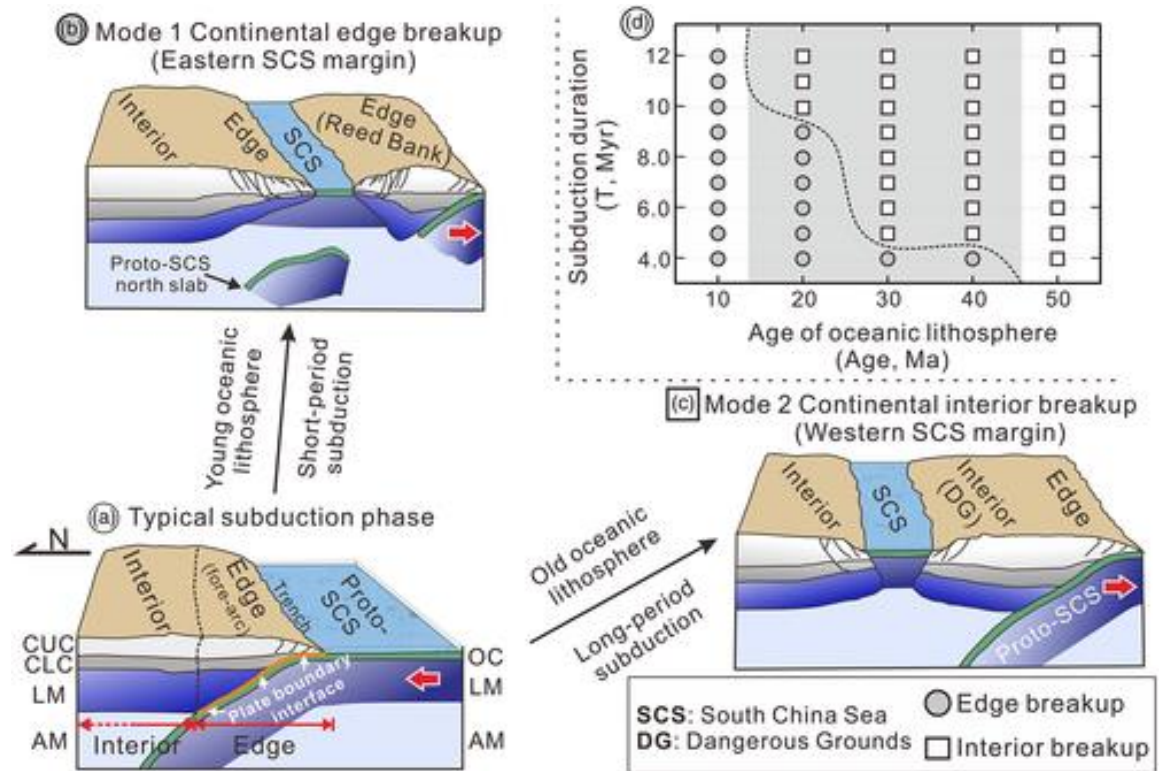

Figure 2. Conceptual models of the contrasting continental breakup modes (a–c) and area diagram summarizing the models in terms of breakup types as a function of subduction duration and age of the oceanic lithosphere (d). (a) Typical subduction zone, in which the upper plate is divided into continental edge and interior according to whether they are located directly above the slab-lithosphere interface. (b, c) Illustration of the breakup of the continental interior and edge, respectively. (d) The dashed line marks the threshold values indicating the transformation from continental edge to interior breakup. The shadow area denotes the conditions under which both breakup modes at a given age can be expected by varying the subduction duration. CUC: continental upper crust; CLC: continental lower crust; LM: lithospheric mantle; AM: asthenospheric mantle; OC: oceanic crust.
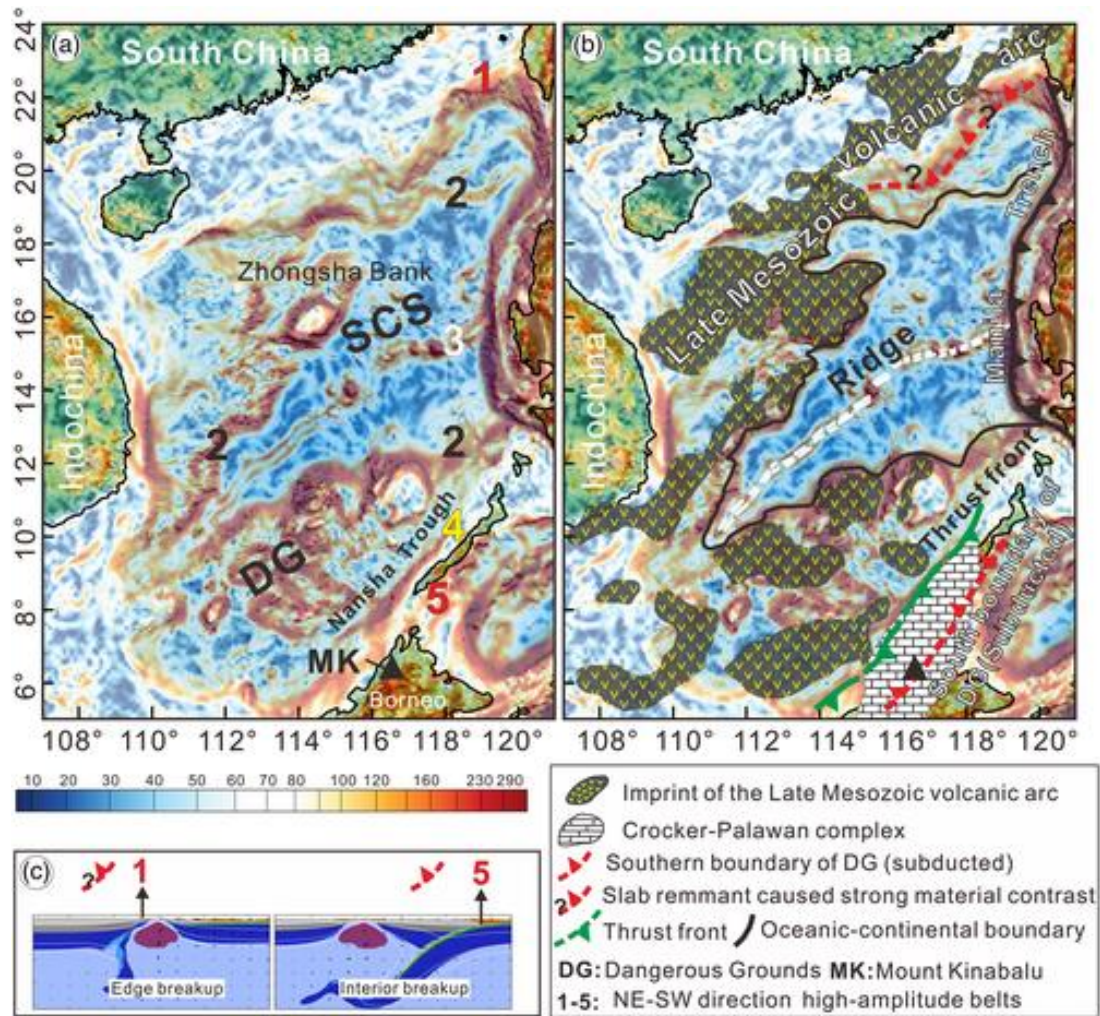
Figure 3. Map of the horizontal gradient of the Bouguer anomaly in the SCS region without (a) and with (b) interpretation and (c) the numerical models used for comparison. High-amplitude anomaly belts paralleling to the South China continental margin are numbered. The region of the Crocker-Palawan complex is modified after Hutchison (2004). The free-air gravity anomaly data are obtained from the satellite-derived field produced by Sandwell et al. (2014). Terrain corrections for Bouguer gravity anomalies are derived from 1′ ×1′ resolution ETOPO1 model (Amante & Eakins, 2009). Nansha Trough (NW Borneo trough), Nansha (Dangerous Grounds).

7. 中国黄土磁化率通量：一种东亚季风降水的新指标

翻译人：杨会会 11849590@mail.sustech.edu.cn

摘要： 中国黄土高原上黄土-古土壤序列的磁化率（χ），作为一种东亚夏季风降水变率的指标已经被广泛应用。这些记录典型地揭示出～100 ka轨道尺度偏心率的强烈气候驱动，但是岁差（～23 ka）驱动相比于深海沉积物的氧同位素记录却要弱。这是令人困惑的，因为季风应该是对岁差变化高度敏感的。我们认为，岁差信号的缺乏是由于磁化率(χ)是一种浓度指标，它受到粉尘沉积速率对降水速率缓释作用的强烈影响。磁化率通量从其他方面矫正了粉尘堆积速率和总浓度影响，更好地揭示了与降水相关的成壤矿物自生速率。在本次研究中，我们将三条 600 ka 来自中国黄土高原的黄土成壤磁化率通量记录与中国石笋氧同位素记录及一条也被用作季风降水指标的 550 ka 宝鸡黄土-古土壤序列 Be 通量记录进行了对比。成壤磁化率通量展示出了清晰的轨道岁差信号，而磁化率 χ（浓度）就没有。

Abstract: Magnetic susceptibility (χ) of loess-paleosol sequences on the Chinese Loess Plateau (CLP) has been widely used as a proxy for East Asian summer monsoon (EASM) precipitation variability. Such records typically show strong climate forcing in the ~100 ka orbital eccentricity band, but exhibit weak processional (~23 ka) forcing relative to that seen in oxygen isotopes from marine sediments. This is puzzling as monsoons should be highly sensitive to precession variations. We assert that this lack of processional signal is because χ is a concentration, which is strongly affected by the dilution effect of dust sedimentation rate superimposed on rainfall rate. χ-flux on the other hand corrects for dust accumulation rate and bulk density effects to better reveal pedogenic mineral ingrowth rates associated with rainfall. In this study, we compare three 600 ka records of loess pedogenic χ-flux from the CLP with Chinese speleothem $\delta^{18}O$ records and a 550 ka loess-

paleosol [10]Be flux record from Baoji which has also been used as a monsoon precipitation proxy record. Pedogenic χ-flux exhibits clear signals of orbital precession, whereas χ (-concentration) does not.
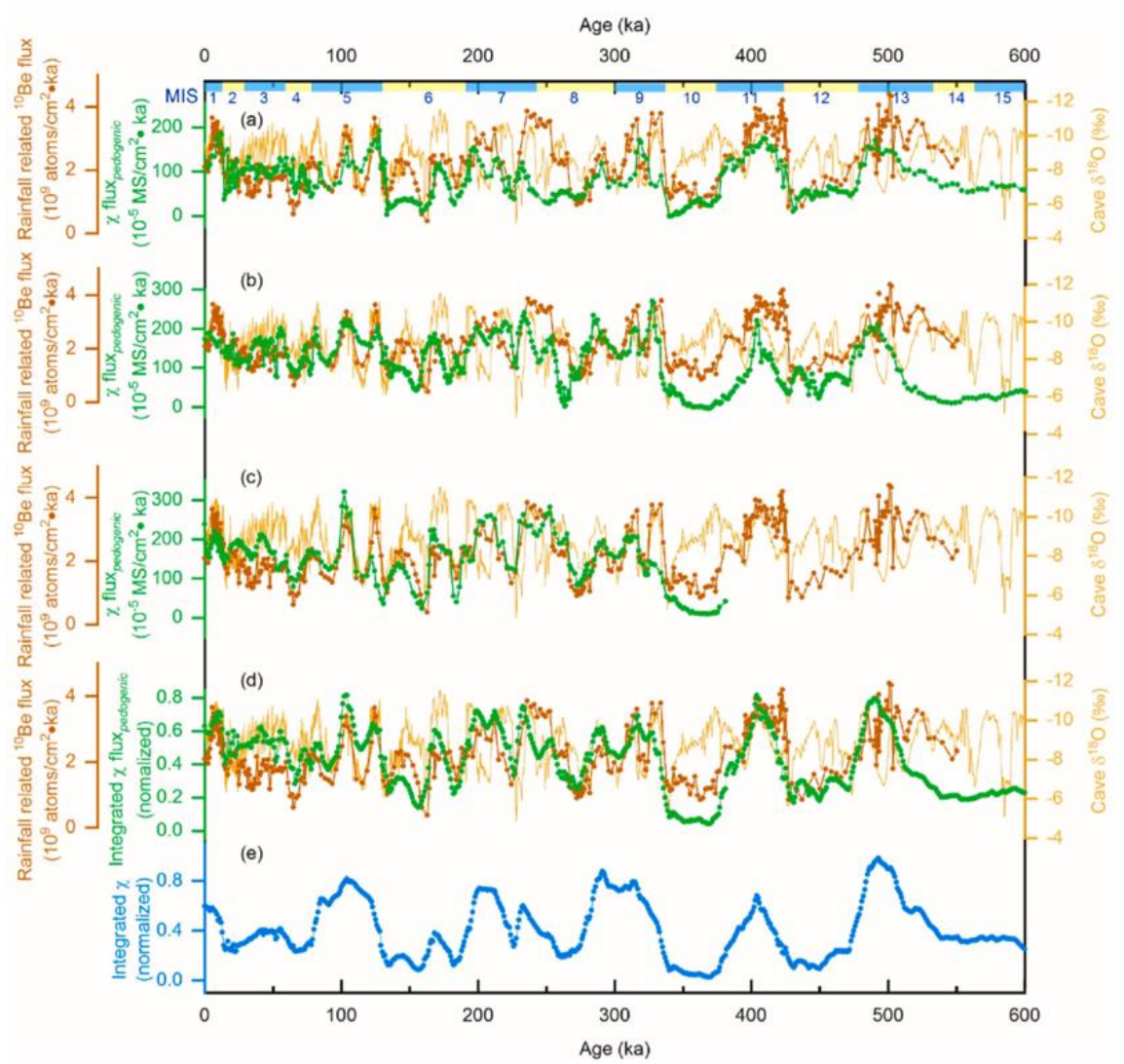

Figure 1. Chinese loess pedogenic χ pedogenic-flux (green) versus Baoji loess [10]Be flux (red) and Sanbao Cave δ^{18}O record (yellow). (a) Luochuan (LC) loess section. (b) Lingtai (LT) loess section. (c) Baoji (BJ) loess section. (d) Integrated χpedogenic-flux (normalized) (green) of Luochuan, Baoji and Lingtai sections. (e) Integrated χ-concentration records (normalized) (blue). The yellow and blue bars with numbers on the top indicate marine isotope stages (MIS). (For interpretation of the references to colour in this figure legend, the reader is referred to the web version of this article.
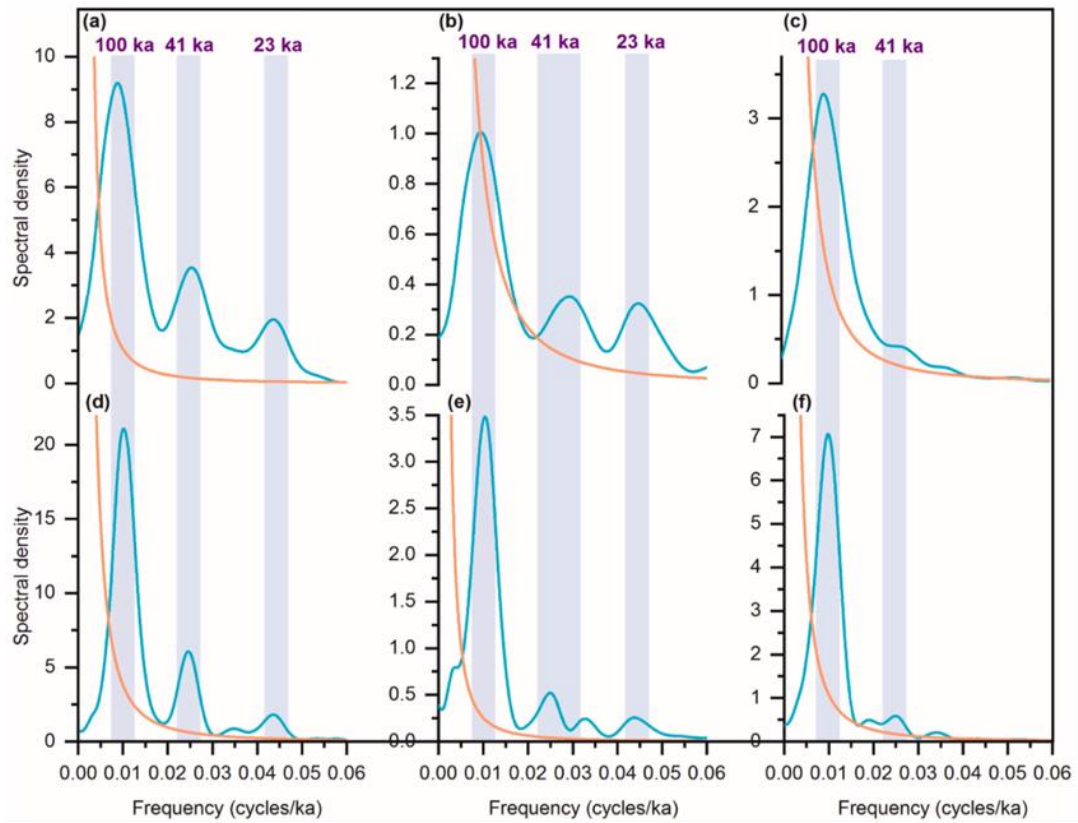
Figure 2. Spectral results of integrated χ pedogenic-flux, benthic δ^{18}O and integrated χ. (a) 0–350 ka benthic δ^{18}O record; (b) 0–350 ka integrated χ pedogenic-flux record; (c) 0–350 ka integrated χ-concentration record; (d) 0–600 ka benthic δ^{18}O record; (e) 0–600 ka integrated χ pedogenic-flux record; (f) 0–600 ka integrated χ-concentration record.

8. LGM 期间亚洲中部，东部和格陵兰岛粉尘不同步累积模式的驱动机制

翻译人：张亚南 zhangyn3@mail.sustech.edu.cn

摘要：我们采集了中亚地区 143 个在 10ka - 30ka 的光释光年龄样品，并分析了它们的概率密度函数（PDFs）。PDFs 结果表明 LGM 末期（23-19 ka）粉尘的累积比 LGM 早期（26.5 - 23ka）更为显著。中亚黄土区粉尘积累时间变化规律与中国黄土高原（CLP）相似。与之相反的是，格陵兰岛的粉尘积累在 LGM 早期相比 LGM 末期更为显著。有实验模拟和我们最新的光释光年龄，我们认为中亚和中国黄土高原在 LGM 粉尘积累受控于与岁差有关的西伯利亚高原强迫；而格陵兰岛的粉尘累积则与倾角周期的夏季西风带强迫和岁差周期的源区粉尘的侵蚀强度有关。

ABSTRACT: We collected 143 loess optically stimulated luminescence (OSL) ages between 10 ka and 30 ka from Central Asia (CA), and analyzed their probability density functions (PDFs). The PDFs show dust accumulation was greater during the late Last Glacial Maximum (LGM) (23–19 ka) than that during the early LGM (26.5–23 ka). The temporal variability of dust accumulation of CA loess is generally similar to that of Chinese Loess Plateau (CLP) loess, following precession. In contrast, dust accumulation in Greenland was stronger during the early LGM than that during the late LGM, following obliquity. Supported by numerical modeling experiments and our newly dating OSL ages, we conclude dust accumulation in CA and CLP during the LGM was controlled by Siberian High forced by precession, while dust accumulation in Greenland was closely related to both intensity of summer westerlies forced by obliquity, and to intensity of dust emissions at source forced by precession.
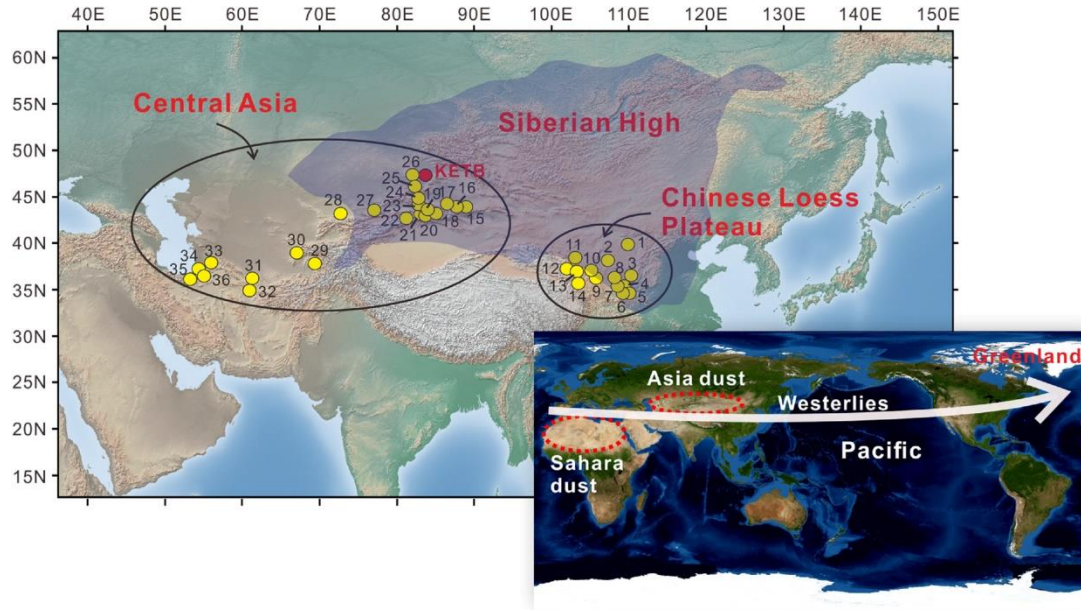
Figure 1. The loess sections in the CA and CLP and range of the modern SH. The range of the modern SH is modified from Zhang et al. (2015). Loess sections (1–14) on the CLP are from Kang et al. (2015) and Table S1 presents detailed information on loess sections (15–36) from the CA. KETB loess section, located in Tacheng Basin, was presented in this study. CA, Central Asia; CLP, Chinese Loess Plateau; SH, Siberian High.
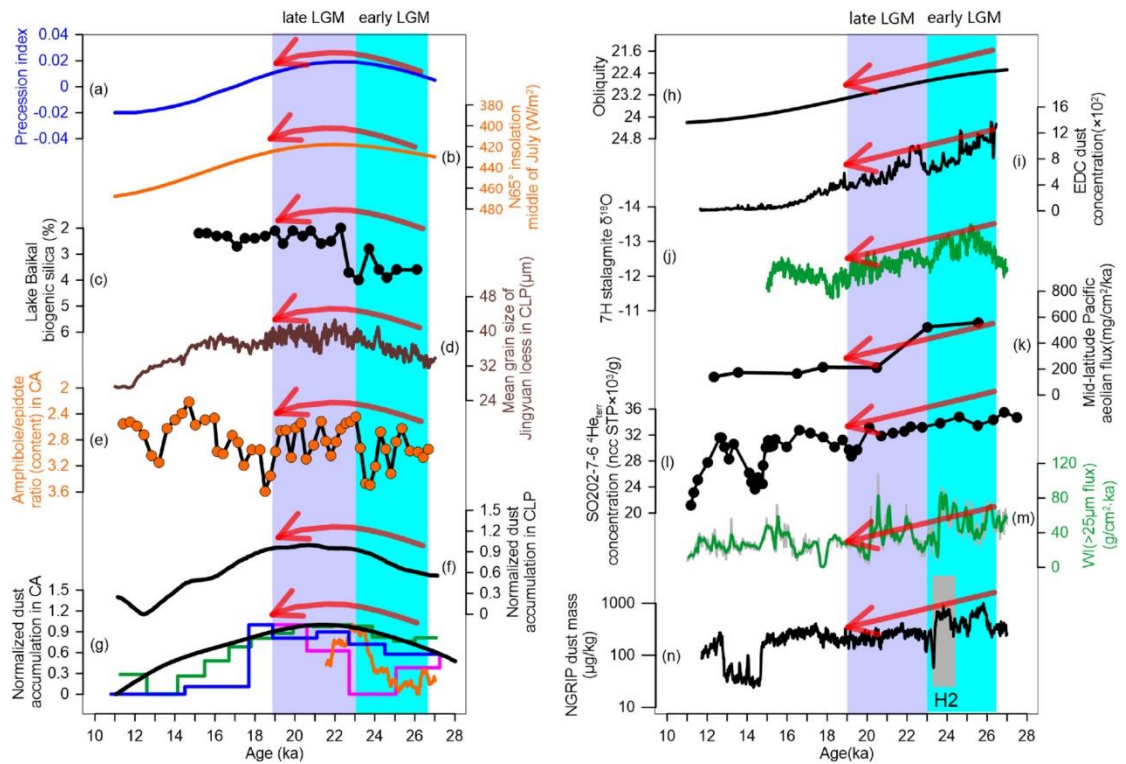

Figure 2. (a), (b) Comparisons between precession index and NHSI at 65°N for July (Berger & Loutre,

1991); (c) Lake Baikal biogenic silica content (Prokopenko et al., 2006); (d) mean grain size for Jingyuan loess (Sun et al., 2012); (e) amphibole/epidote ratio for Xiaoerbulake loess (Cheng et al., 2020); (f) normalized PDF from 159 OSL ages for loess from the CLP (Kang et al., 2015); and (g) normalized PDF (black) from 143 OSL ages for loess from CA, with normalized sedimentation rate for sections: Xiaoerbulake (green) (Cheng et al., 2020), Hoalin (orange) (Wang et al., 2018), Remizovka (magenta) (Fitzsimmons et al., 2018), Kansu15‐05 (blue) (Wang et al., 2019); (h) Obliquity (Berger & Loutre, 1991); (i) dust concentration in an Antarctic ice core (Lambert et al., 2008); (j) stalagmite δ18O from Cave 7H in Bernese Alps, Switzerland (Luetscher et al., 2015); (k) aeolian dust flux to the midlatitude North Pacific Ocean, using V21‐146 SPECMAP age scale (Hovan et al., 1989); (l) 4Heterr concentration records from SO202‐7‐6 (Serno et al., 2015); (m) index for westerlies (An et al., 2012); (n) dust concentrations from NGRIP ice core, using GICC05 age scale (Ruth et al., 2007). CLP, Chinese Loess Plateau; NHSI, northern hemisphere summer insolation; PDF, probability density function.
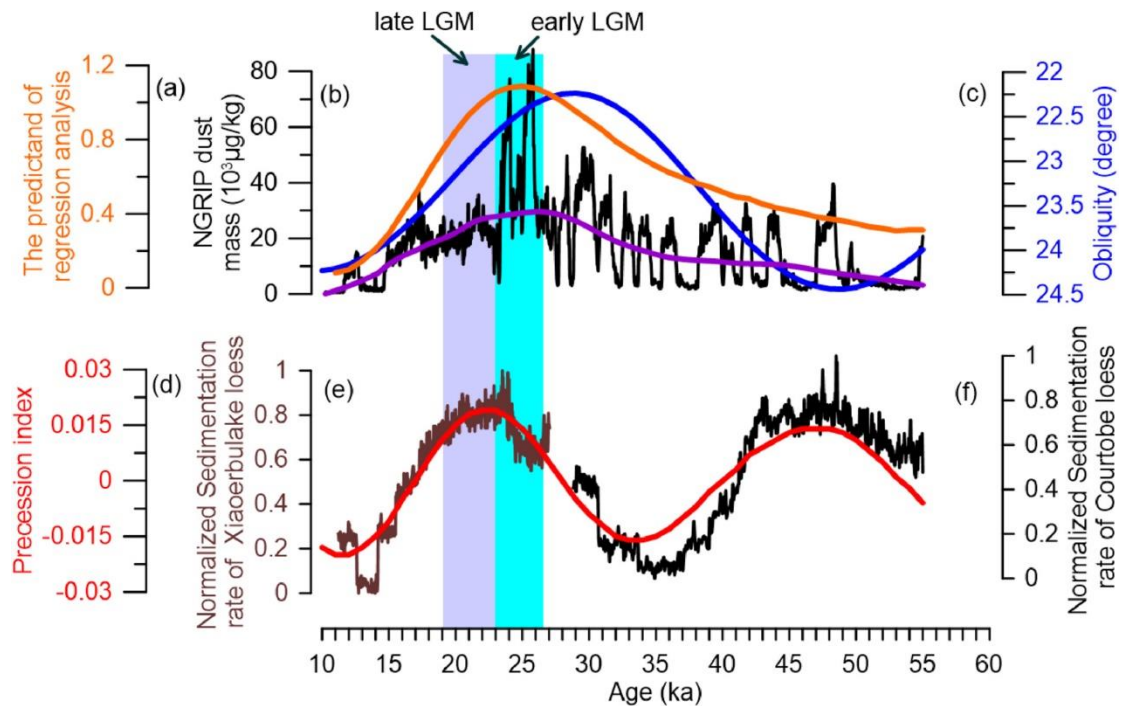

Figure 3. (a) The predictand of regression analysis; (b) dust concentration from NGRIP ice core (black), using GICC05 age scale (Ruth et al., 2007) with 30% LOWESS detrended curve (purple, conducted in Acycle version 2.2 [Li, Hinnov, et al., 2019]); (c), (d) obliquity and precession (Berger & Loutre, 1991); (e), (f) normalized sedimentation rates for Xiaoerbulake (Cheng et al., 2020) and Courtobe (Figure S5) loess sections.

9. 磁性地层约束印度-亚洲碰撞对西藏东南缘贡觉盆地的同步沉积作用

翻译人：李海 12031330@mail.sustech.edu.cn

摘要: 数十年来，印度与亚洲的碰撞一直是争论的焦点，其起始年龄从晚白垩纪至渐新世。在近场和远场环境中保存的沉积记录为碰撞的年龄和机制提供了关键的证据。贡觉盆地是青藏高原东部边缘发育的一系列断层控制盆地之一，其沉积序列出露明显，为研究印度-亚洲碰撞和高原隆升的沉积、构造-地貌和气候历史提供了巨大的潜力。岩相分析表明，该层序主要由河流相湖盆系砂岩、泥岩和砾岩组成。高分辨率地层学受到首次在贡觉盆地中部发现的火山碎屑层中锆石的 U-Pb 年代的约束，表明沉积始于 69 Ma（C31n），并在该地区持续到 50 Ma（C22r）。基于年龄框架的磁化率各向异性（AMS）解释揭示了 50 Ma 以来沉积后的挤压，同时响应了印度-亚洲碰撞带动的青藏高原东南部的早期隆升。

Abstract: The India-Asia collision has been the object of vigorous debate for decades, with ages of the start ranging from Late Cretaceous to Oligocene. Sedimentary records preserved in both near-field and far-field settings provide critical evidence concerning the age and mechanism of the collision. Gonjo Basin, one of a series of fault-controlled basins developed along the eastern margin of Tibetan Plateau, contains well-exposed sedimentary successions, providing great potential for understanding depositional, tectonic-geomorphological and climatic history associated with India-Asia collision and plateau uplift. Lithofacies analysis reveals that the sequences consist of sandstone, mudstone and conglomerate, formed in fluvial-lacustrine systems. High-resolution magnetostratigraphy, constrained by U-Pb dating of zircon from a volcaniclastic layer which has been found in the central Gonjo Basin for the first time, indicates that sedimentation started at 69 Ma (C31n) and continued in this locality until 50 Ma (C22r). Anisotropy of magnetic susceptibility (AMS) interpretation based on the age framework reveals a post-depositional compression after 50 Ma, responding simultaneously to the early uplift of southeast Tibetan Plateau driven by India-Asia collision.
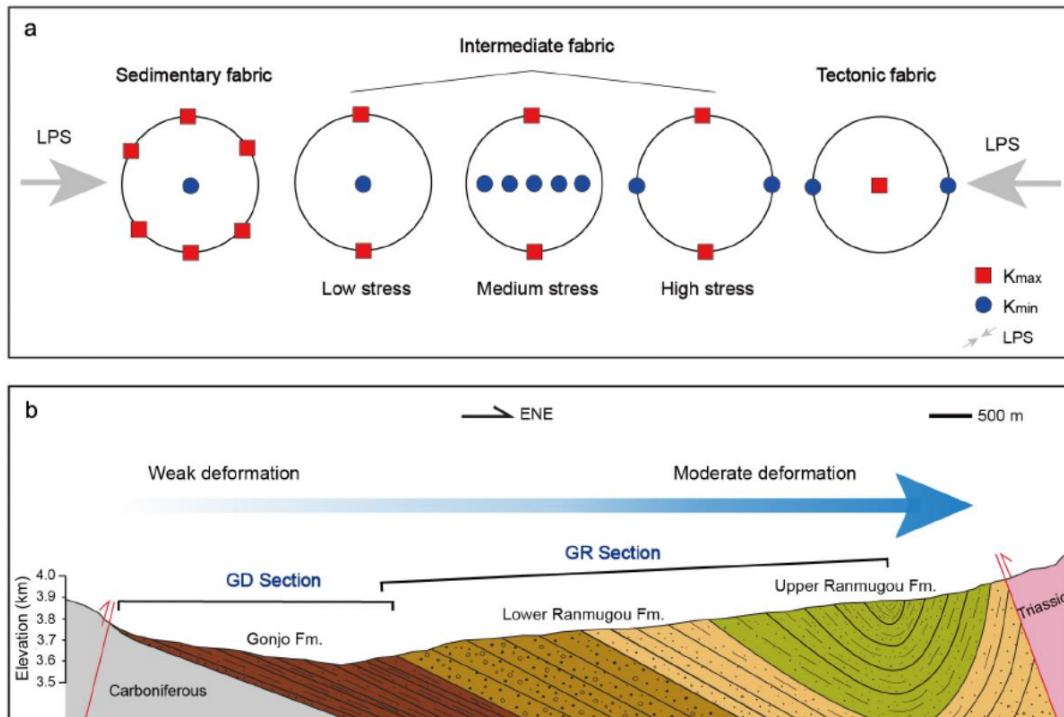
Figure 1. Evolution from a sedimentary fabric to a tectonic fabric under progressive deformation (layer parallel shortening, LPS) (a). Deformation visible in cross sections through the center of Gonjo Basin (b).
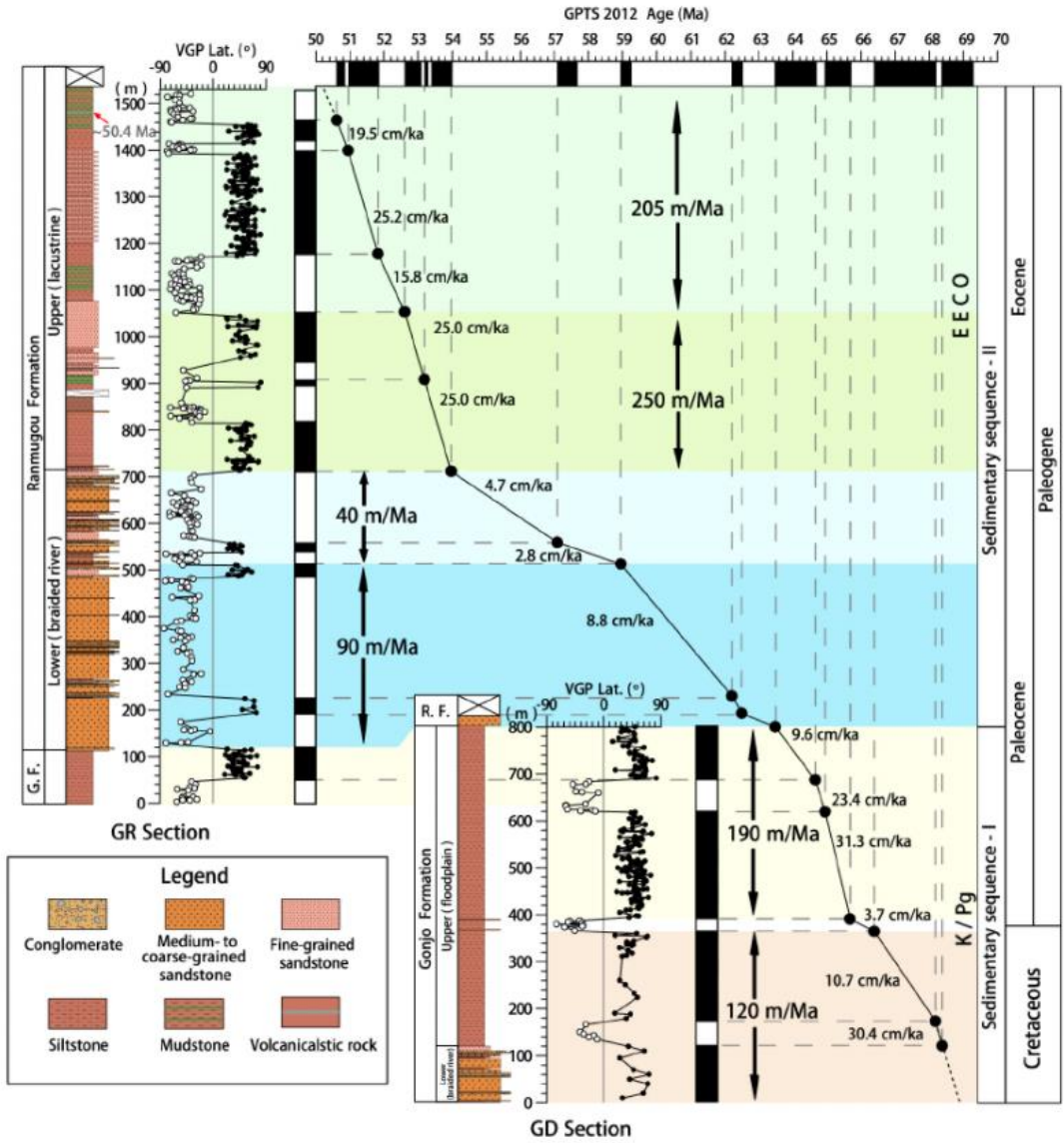
Figure 2. Age-depth-accumulation of Gonjo Basin with geomagnetic polarity timescale (GPTS) (Ogg, 2012). Schematic stratigraphic columns of the GD and GR sections are shown by the side of paleomagnetic results.

10. ENSO 在东亚夏季风与冬季风联系中的作用

翻译人：郑威　11930589@mail.sustech.edu.cn

摘要：本文研究了东亚夏季风与随后的东亚冬季风之间的联系。结果表明，东亚夏季风强（弱）的年份往往东亚冬季风也强（弱），说明了东亚夏季风向东亚冬季风同相的转变主导了它们之间的联系。强东亚夏季风向强东亚冬季风的转变是基于西北太平洋上一个夏季的异常反气旋和一个冬季的异常气旋。弱东亚夏季风向弱东亚冬季风转变的联系方式与强季风同理，西北太平洋夏季出现异常气旋，冬季出现异常反气旋。进一步研究表明，ENSO在东亚夏季风向东亚冬季风同相转变的过程中有关键作用，通过引起Rossby波对ENSO导致的对流异常的响应来驱动西北太平洋夏季异常气旋向冬季异常反气旋的转变。数值模拟分析进一步证实了ENSO在东亚夏季风向东亚冬季风同相转变中的主导作用。不对称分析表明，东亚夏季风向东亚冬季风的同相转变相较于拉尼娜事件，对厄尔尼诺事件的响应更强。

ABSTRACT: The link between the East Asian summer monsoon (EASM) and the ensuing East Asian winter monsoon (EAWM) is investigated. The results found that strong (weak) EASM years are often followed by the strong (weak) EAWM years, demonstrating that the in-phase EASM to EAWM transition dominate the EASM-EAWM link. The strong EASM to the strong EAWM transition is established by an anomalous anticyclone over the western North Pacific (WNPAC) in summer and an anomalous cyclone (WNPC) in winter. The weak EASM to the weak EAWM transition is connected by the same way but with the WNPC in summer and the WNPAC in winter. Further studies suggest that ENSO plays a crucial role in the in-phase EASM to EAWM transition, which forces the transition between the WNPC and WNPAC from summer to winter via inducing Rossby wave responses to the ENSO-induced convection anomalies. Numerical simulation analysis

further confirms the dominant role of ENSO in the in-phase EASM to EAWM transitions. The asymmetric analysis suggests that the in-phase EASM to EAWM transition is stronger under El Niño than under La Niña.
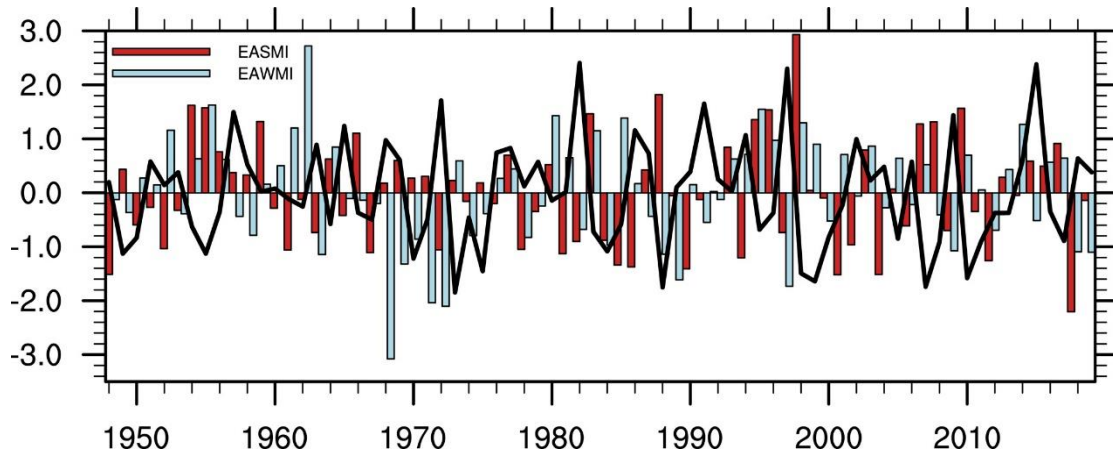

Figure 1. Normalized summer (JJA) mean EASM index, winter (DJF) mean EAWM index, and Niño3.4 index for the period 1948–2019. DJF, December-January-February; JJA, June-July-August; SON, September-October-November.

11. 理解火成岩非理想古强度记录：熔岩样品老化实验的见解和 Arai 图"脆弱"曲率的原因及影响

翻译人：张伟杰 12031188@mail.sustech.edu.cn

摘要：热阻挡剩磁理论预测了岩石冷却过程中施加的低场（如地磁场）与获得的磁化呈准线性关系。这是评估古代地磁场强度的基础。解决长期存在的关于地球磁场的问题需要一个全球的古强度数据集，但恢复古磁场强度是复杂的，因为理论只适用于均匀磁化的粒子。古强度实验的一个关键要求是在给定温度下阻挡的磁化应通过零场再加热到相同温度来解阻。然而，这一要求的失败经常发生，而且失败的原因和后果并不完全了解。最近的实验表明，在许多典型的古强度实验样品中，剩磁是不稳定的，表现出一种"老化"效应，即阻挡/解阻温度谱在短短几年内就会发生变化，从而导致非理想的实验行为。新鲜的剩磁可能符合阻挡和解阻温度相等的要求，而老的剩磁可能不符合。阻挡温度谱可能是不稳定的(脆弱的)，这就阻碍了原始磁化条件的再现。这限制了我们获取精确的古代磁场强度估计的能力，因为已知和估计的磁场之间的差异对于单个样本来说是显著的。解封温度谱的脆弱性可能与具有较低能垒尺寸的磁性颗粒有关，可以通过一阶反转曲线观察到的特征来检测。

ABSTRACT: The theory for recording of thermally blocked remanences predicts a quasilinear relationship between low fields like the Earth's in which rocks cool and acquire a magnetization. This serves as the foundation for estimating ancient magnetic field strengths. Addressing long-standing questions concerning Earth's magnetic field requires a global paleo-intensity data set, but recovering the ancient field strength is complicated because the theory only pertains to uniformly magnetized particles. A key requirement of a paleo-intensity experiment is that a magnetization

blocked at a given temperature should be unblocked by zero-field reheating to the same temperature. However, failure of this requirement occurs frequently and the causes and consequences of failure are understood incompletely. Recent experiments demonstrate that the remanence in many samples typical of those used in paleo-intensity experiments is unstable, exhibiting an "aging" effect in which the (un)blocking temperature spectra can change over only a few years resulting in nonideal experimental behavior. While a fresh remanence may conform to the requirement of equality of blocking and unblocking temperatures, aged remanences may not. Blocking temperature spectra can be unstable (fragile), which precludes reproduction of the conditions under which the original magnetization was acquired. This limits our ability to acquire accurate and precise ancient magnetic field strength estimates because differences between known and estimated fields can be significant for individual specimens, with a low field bias. Fragility of unblocking temperature spectra may be related to grain sizes with lower energy barriers and may be detected by features observed in first-order reversal curves.
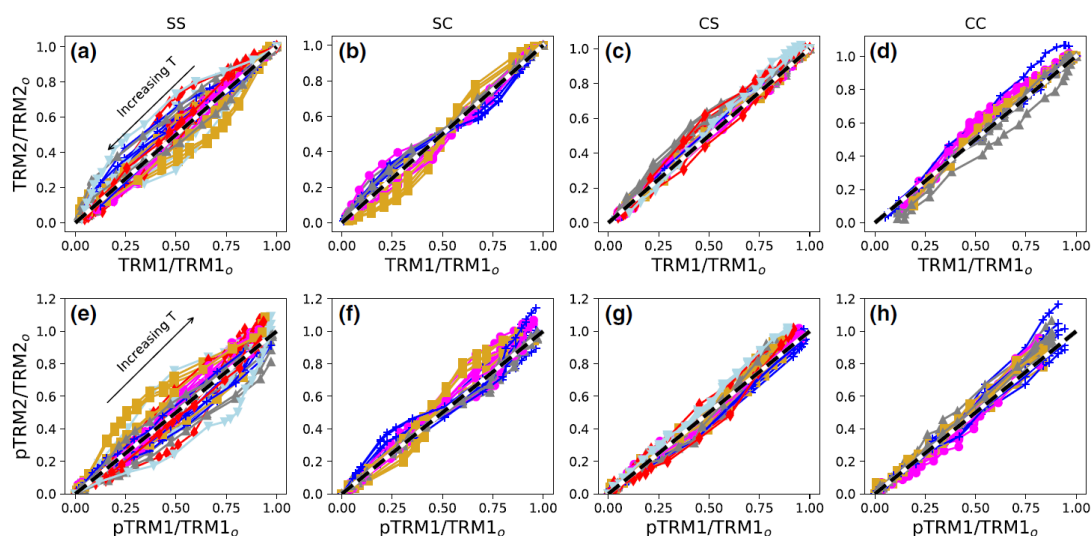

Figure 1. Comparison of (un)blocking temperature spectra between fresh and aged specimens. The curves for demagnetization and remagnetization for the experiments are shown in Figures S2 and S3. The expected line of equal (un)blocking at a given step is shown by the black dashed line in each plot. (a–d) TRM unblocking (zero field steps). X-axis is magnetization remaining at each temperature step for the fresh TRM (TRM1); Y-axis is magnetization remaining for each aged specimen at the same temperature step (TRM2). The initial TRM is at the upper right-hand corner of the plot. (e–h) TRM blocking (infield steps). X-axis is magnetization acquired at each temperature step of the fresh pTRM

(pTRM1); Y-axis is magnetization acquired for each aged specimen at the same temperature step (pTRM2). The final pTRM is at the upper right-hand side of the plot. (a, e) SS group specimens. (b, f) SC group specimens. (c, g) CS group specimens. (d, h) CC group specimens. pTRM, partial TRM; TRM, thermal remanent magnetizations.
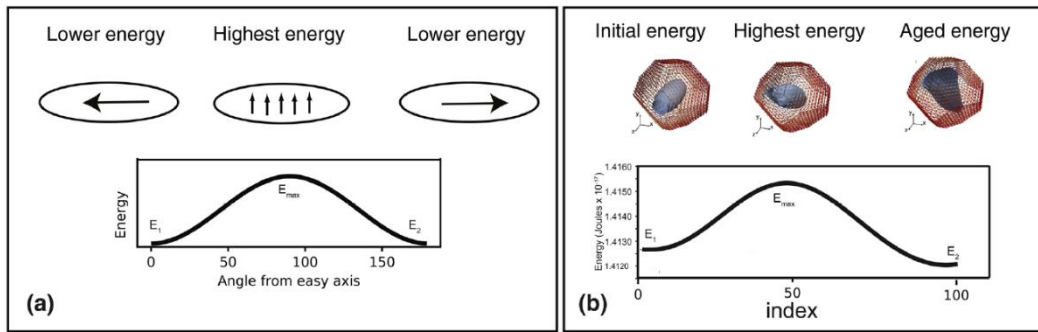

Figure 2. Energy barriers to magnetization switching from one easy axis to the other. (a) Néel particle (uniaxial SD). (b) Single vortex particle with multiple easy axes. SD, Single Domain.

12. 深渊海沟是深海环境成岩作用的动态热点

翻译人：王敦繁　　dunfan_w@foxmail.com

摘要： 全球海洋的最深处--海沟深渊--被认为是有机物质的沉积中心。在一些海沟的最深部分，已经证明了相对较高的微生物活动，但沉积动力学被认为是空间和时间变化的。在这里，我们沿着两个具有对比地表初级生产力的海沟(克马德克海沟和阿塔卡马海沟)探索沉积物特征和原位底栖氧吸收。我们发现，深海底栖的耗氧量在不同地点之间相差约 10 倍，但与邻近的深海平原相比，在所有情况下都有所增加。两个海沟区域的底栖氧气吸收反映了表面产量的差异，而每个海沟内的变化受局部沉积动力学的调节。呼吸活动与有机碳和植物碎屑物质的沉积库存量有关。研究认为深海深沟是早期成岩作用的热点，具有比以往认识的更丰富、更动态的环境。

ABSTRACT: The deepest part of the global ocean, hadal trenches, are considered to act as depocenters for organic material. Relatively high microbial activity has been demonstrated in the deepest sections of some hadal trenches, but the deposition dynamics are thought to be spatially and temporally variable. Here, we explore sediment characteristics and in-situ benthic oxygen uptake along two trenches with contrasting surface primary productivity: the Kermadec and Atacama trenches. We find that benthic oxygen consumption varies by a factor of about 10 between hadal sites but is in all cases intensified relative to adjacent abyssal plains. The benthic oxygen uptake of the two trench regions reflects the difference in surface production, whereas variations within each trench are modulated by local deposition dynamics. Respiratory activity correlates with the sedimentary inventories of organic carbon and phy- todetrital material. We argue that hadal trenches represent deep sea hotspots for early diagenesis and are more diverse and dynamic environments than previously recognized.
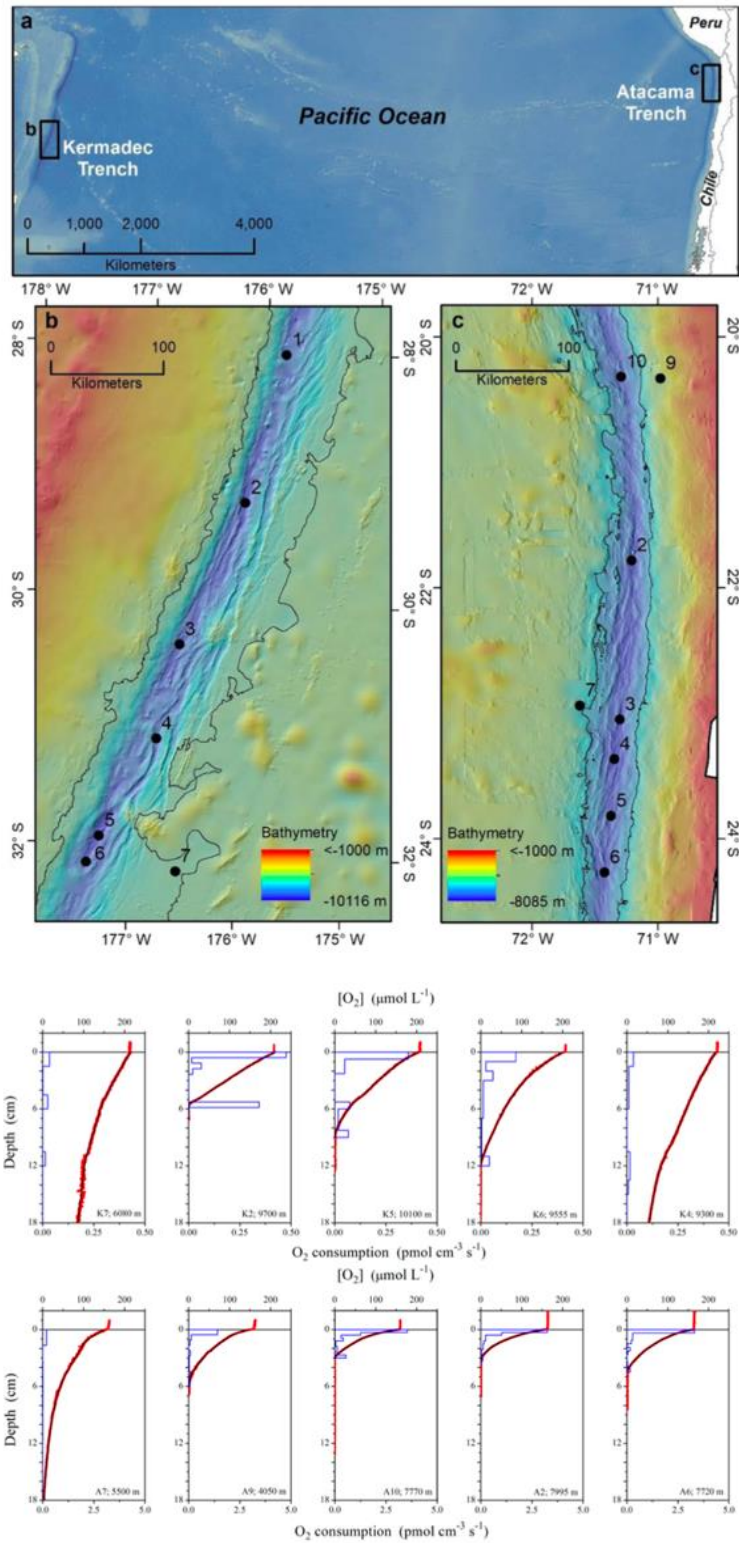
Figure 1: Study areas in the Kermadec Trench and the Atacama Trench regions in the Pacific Ocean. And Selected oxygen microprofiles measured in the Kermadec Trench (K) and Atacama Trench (A) regions.

## 13. 全新世以来，中亚东北部干旱地区近地表风强度的变化

翻译人：王浩森 11930841@mail.sustech.edu.cn

摘要：尘埃源区的风动力学在区域和全球范围内都会受到气候变化的影响。中亚干旱区东北部是亚洲粉尘的最重要来源之一。为了重建近地表风强度的变化，我们对来自中亚干旱区东北部的四个全新世风成沉积序列样品中提取的石英成分进行了粒度分析，并探讨了可能的机制。还进行了 X 射线衍射和地球化学分析。结果表明，在研究区域，风沙沉积物石英成分的平均粒径是近地表风和西伯利亚高压系统强度的更可靠的替代指标。全新世早期至中期出现了更强的近地表风和西伯利亚高压系统，随后逐渐减弱。全新世早期至中期，较低的日辐射量，较低的大气 CO_2 含量以及残留的高纬度大陆冰盖导致北半球中高纬度地区的冬季温度相对较低。较低的冬季温度表明西伯利亚高压系统更强，这可能是近地面风增强的原因。由于冬季日照强度和大气中二氧化碳含量的增加，以及高纬区大陆冰原的收缩，西伯利亚高压系统由于全新世中期至晚期的冬季温度升高而减弱，这可能导致近地表风强度的降低。

ABSTRACT: Wind dynamics in dust source areas are influenced by climate change on both regional and global scales. Northeastern arid central Asia is one of the most important sources of Asian dust. We conducted grain size analyses of the extracted quartz component of bulk samples from four Holocene aeolian sedimentary sequences in northeastern arid central Asia, in order to reconstruct variations in strength of near‑surface wind, and discussed the possible mechanism. X‑ray diffraction and geochemical analyses were also conducted. The results suggest that in the study area the mean grain size of the quartz component of aeolian sediments is a more reliable proxy for the strength of near‑surface wind and Siberian high‑pressure system. Stronger near‑surface wind and Siberian high‑pressure system occurred during the early to middle Holocene and subsequently their gradually weakened. Lower winter insolation, lower atmospheric CO_2 content,

and remnant high‑latitude continental ice‑sheets resulted in relatively low winter temperatures in middle and high latitudes of the Northern Hemisphere during the early to middle Holocene. The lower winter temperatures indicate a stronger Siberian high‑pressure system, which may have been the cause of the stronger near‑surface winds. Due to increasing winter solar insolation and atmospheric CO_2 content, and the shrinking high‑latitude continental ice‑sheets, the Siberian high‑pressure system weakened in response to rising winter temperatures during the middle to late Holocene, likely resulting in decreased near‑surface wind strength.
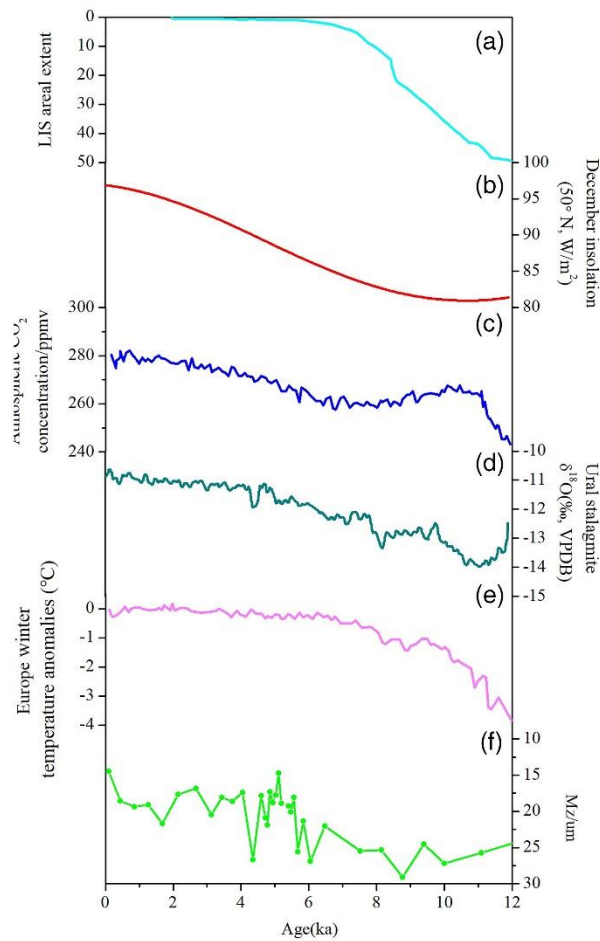
Figure 7. Area of the Laurentide ice sheet (a); December insolation at 50°N (b); Atmospheric CO_2 concentration (c); Speleothem oxygen isotope record from the Urals, reflecting changes in winter temperature (d); Pollen-based reconstructed area-averaged winter temperature of Europe (e); Trend of near-surface wind strength evolution indicated by the grain size of the quartz component of the LJW10 loess-paleosol sequence (f).